

# Exploring the partonic phase at finite chemical potential within an extended off-shell transport approach

Pierre Moreau,<sup>1,\*</sup> Olga Soloveva,<sup>1</sup> Lucia Oliva,<sup>1,2</sup> Taesoo Song,<sup>2</sup> Wolfgang Cassing,<sup>3</sup> and Elena Bratkovskaya<sup>1,2</sup>

<sup>1</sup>*Institute for Theoretical Physics, Johann Wolfgang Goethe-Universität, Frankfurt am Main, Germany*

<sup>2</sup>*GSI Helmholtzzentrum für Schwerionenforschung GmbH, Darmstadt, Germany*

<sup>3</sup>*Institut für Theoretische Physik, Universität Gießen, Germany*

We extend the Parton-Hadron-String Dynamics (PHSD) transport approach in the partonic sector by explicitly calculating the total and differential partonic scattering cross sections as a function of temperature  $T$  and baryon chemical potential  $\mu_B$  on the basis of the effective propagators and couplings from the Dynamical QuasiParticle Model (DQPM) that is matched to reproduce the equation of state of the partonic system above the deconfinement temperature  $T_c$  from lattice QCD. We calculate the collisional widths for the partonic degrees of freedom at finite  $T$  and  $\mu_B$  in the time-like sector and conclude that the quasiparticle limit holds sufficiently well. Furthermore, the ratio of shear viscosity  $\eta$  over entropy density  $s$ , i.e.  $\eta/s$ , is evaluated using the collisional widths and compared to lQCD calculations for  $\mu_B = 0$  as well. We find that the novel ratio  $\eta/s$  does not differ very much from that calculated within the original DQPM on the basis of the Kubo formalism. Furthermore, there is only a very modest change of  $\eta/s$  with the baryon chemical  $\mu_B$  as a function of the scaled temperature  $T/T_c(\mu_B)$ . This also holds for a variety of hadronic observables from central A+A collisions in the energy range  $5 \text{ GeV} \leq \sqrt{s_{NN}} \leq 200 \text{ GeV}$  when implementing the differential cross sections into the PHSD approach. We only observe small differences in the antibaryon sector ( $\bar{p}$ ,  $\bar{\Lambda} + \bar{\Sigma}^0$ ) at  $\sqrt{s_{NN}} = 17.3 \text{ GeV}$  and  $200 \text{ GeV}$  with practically no sensitivity of rapidity and  $p_T$  distributions to the  $\mu_B$  dependence of the partonic cross sections. Small variations in the strangeness sector are obtained in all studied collisional systems (A+A and C+Au), however, it will be very hard to extract a robust signal experimentally. Since we find only small traces of a  $\mu_B$ -dependence in heavy-ion observables - although the effective partonic masses and widths as well as their partonic cross sections clearly depend on  $\mu_B$  - this implies that one needs a sizable partonic density and large space-time QGP volume to explore the dynamics in the partonic phase. These conditions are only fulfilled at high bombarding energies where  $\mu_B$  is, however, rather low. On the other hand, when decreasing the bombarding energy and thus increasing  $\mu_B$ , the hadronic phase becomes dominant and accordingly, it will be difficult to extract signals from the partonic dynamics based on "bulk" observables.

PACS numbers: 12.38.Mh, 25.75.-q, 25.75.Nq

## I. INTRODUCTION

Non-equilibrium many-body theory or transport theory has become a major topic of research in nuclear physics, in cosmological particle physics as well as condensed matter physics. The multidisciplinary aspect arises due to a common interest to understand the various relaxation phenomena of quantum dissipative systems. Important questions in nuclear and particle physics at the highest energy densities are: i) how do non-equilibrium systems in extreme environments evolve and eventually thermalize, ii) what are the macroscopic transport coefficients of the matter in equilibrium and iii) what is the nature of possible phase transitions? The dynamics of heavy-ion collisions at various bombarding energies provide the laboratory of choice for research on non-equilibrium quantum many-body physics and relativistic quantum-field theories, since the initial state of a collision resembles an extreme non-equilibrium configuration while the final state might even exhibit some degree of thermalization.

Since many decades the powerful method of the ‘Schwinger-Keldysh’ [1–4] or ‘closed time path’ (CTP) real-time Green’s functions – being the essential degrees-of-freedom – has been shown to provide an appropriate basis for the formulation of the complex problems in the various areas of non-equilibrium quantum many-body physics. Within this framework one can derive suitable approximations - depending on the problem under consideration - by preserving overall consistency relations [5]. Originally, the resulting causal Dyson-Schwinger equation of motion for the one-particle Green’s functions (or two-point functions), i.e. the Kadanoff-Baym (KB) equations [6], have served as the underlying scheme for deriving various transport phenomena and generalized transport equations. For review articles on the Kadanoff-Baym equations in the various areas of non-equilibrium quantum physics we refer the reader to Refs. [7–12].

On the other hand, kinetic transport theory is a convenient method to study many-body non-equilibrium systems. Kinetic equations, which do play the central role in more or less all practical simulations, can be derived from the KB equations within suitable approximations. Hence, a major impetus in the past has been to derive semi-classical Boltzmann-like transport equations within

\* moreau@fias.uni-frankfurt.de

the standard quasiparticle approximation. Additionally, off-shell extensions by means of a gradient expansion in the space-time inhomogeneities - as already introduced by Kadanoff and Baym [6] - have been formulated for various directions in physics: from a relativistic electron-photon plasma [13] to the transport of nucleons at intermediate heavy-ion reactions [14] to the transport of partons in high-energy heavy-ion reactions [15–23]. We recall that on the formal level of the KB-equations the various forms assumed for the self-energy have to fulfill consistency relations in order to preserve symmetries of the fundamental Lagrangian [6, 24, 25]. This allows for a unified treatment of stable and unstable (resonance) particles also out-of-equilibrium.

The perspectives to solve in particular QCD in Minkowski space for out-of-equilibrium configurations and non-vanishing quark (or baryon) densities will be low also in the next years such that effective approaches are necessary to model the dominant properties of QCD in equilibrium, i.e. the thermodynamic quantities as well as transport coefficients. To this aim the Dynamical Quasi-Particle Model (DQPM) has been introduced [26] which is based on partonic propagators with sizable imaginary parts of the selfenergies incorporated. Whereas the real part of the self-energies can be attributed to a dynamically generated mass (squared) the imaginary parts contain the information about the interaction rates in the system [27–34]. Furthermore, the imaginary parts of the propagators define the spectral functions of the degrees of freedom which might show narrow (or broad) quasiparticle peaks [35]. A further advantage of a propagator based approach is that one can formulate a consistent thermodynamics [36] as well as a causal theory for non-equilibrium configurations on the basis of KB equations.

In order to explore the phase diagram of strongly interacting matter as a function of temperature  $T$  and baryon chemical potential  $\mu_B$  different strategies are employed at present: i) lattice calculations of quantum chromodynamics (lQCD) [37–39] show that the phase transition from hadronic to partonic degrees of freedom (at vanishing baryon chemical potential  $\mu_B = 0$ ) is a crossover. This phase transition is expected to turn into a first order transition at a critical point  $(T_r, \mu_r)$  in the phase diagram with increasing baryon chemical potential  $\mu_B$  [40–42]. Since this critical point cannot be determined theoretically in a reliable way by lQCD calculations, experimental information from relativistic nucleus-nucleus collisions has to be obtained. In this respect ii) the beam energy scan (BES) program - performed at the relativistic heavy-ion collider (RHIC) - aims to find the critical point and the phase boundary by gradually decreasing the collision energy [43, 44] and thus increasing the average baryon chemical potential. Additionally, new facilities such as FAIR (Facility for Antiproton and Ion Research) and NICA (Nuclotron-based Ion Collider facility) are under construction to explore in particular the intermediate energy range of  $4 \text{ GeV} \leq \sqrt{s_{NN}} \leq 20 \text{ GeV}$  where one might study also the competition between chi-

ral symmetry restoration and deconfinement [45, 46].

Accordingly, the partonic and hadronic dynamics at finite/large baryon densities (or chemical potentials) are of actual interest and are addressed also in various hydrodynamical models [47–50], hydrodynamical + hadron transport models [51, 52] or more parametric approaches [53]. However, as found in Ref. [51], the inclusion of baryon diffusion leads only to a small effect on the "bulk" observables at BES RHIC energies.

About a decade ago the Parton-Hadron-String Dynamics (PHSD) transport approach has been introduced, which differs from the conventional Boltzmann-type models in the aspect [54] that the degrees-of-freedom for the QGP phase are off-shell massive strongly-interacting quasiparticles that generate their own mean-field potential. The masses of the dynamical quarks and gluons in the QGP are distributed according to spectral functions whose pole positions and widths, respectively, are defined by the real and imaginary parts of their self-energies [55]. The partonic propagators and self-energies, furthermore, are defined in the DQPM in which the strong coupling and the self-energies are fitted to lattice QCD results [26] assuming an ansatz for the mass and width dependencies on temperature  $T$  and quark chemical potential  $\mu_q$  inspired by the Hard-Thermal-Loop (HTL) approach.

In the past the PHSD transport model, based on temperature dependent DQPM masses, widths and cross sections [56], has successfully described numerous experimental data in relativistic heavy-ion collisions from the Alternating Gradient Synchrotron (AGS), Super-Proton-Synchrotron (SPS), RHIC to Large Hadron Collider (LHC) energies [54, 55, 57–62].

The *goal of this study* is to explore on a microscopic level the partonic phase at finite baryonic chemical potential  $\mu_B$  and different temperatures  $T$ , and find traces of the  $\mu_B$  dependence in observables. In spite that the extension of the DQPM model to finite baryon chemical potentials has been realized previously [63, 64] and the  $(T, \mu_B)$ -dependence of the transport coefficients (such as shear and bulk viscosities or electric conductivity) for the equilibrated QGP matter have been calculated [63, 64], the properties of the non-equilibrium QGP at finite  $\mu_B$  - as created in heavy-ion collisions (HICs) - were not addressed by microscopic calculations within the PHSD so far in a consistent fashion.

Although the DQPM inherits the information on the total interaction rates of the degrees of freedom in terms of widths it lacks the individual total as well as differential cross sections for different reaction channels with partons that are needed in the collision terms of a consistent relativistic transport approach. In PHSD these cross sections have been parametrized so far to comply with the individual widths of quarks, antiquarks and gluons as a function of energy density (cf. Ref. [56]) which can be related to the temperature  $T$  by the lQCD equation of state (EoS). In this study we will calculate these total and differential cross sections in leading order for the individual partonic channels on the basis of the DQPM

propagators and couplings. This will allow to explore the energy and angular dependence of partonic cross sections additionally on their  $T$  and  $\mu_B$  dependence.

Moreover, using these cross sections, we calculate the interaction rates of quarks and gluons in the time-like sector to study the validity of the quasiparticle approximation. Furthermore, we evaluate the equilibrium shear viscosity  $\eta(T, \mu_B)$  within the Kubo formalism and the relaxation time approximation (RTA) and compare to results from lQCD at  $\mu_B = 0$  for the ratio  $\eta/s$ . The calculated total and differential cross sections as well as parton masses - depending on  $(T, \mu_B)$  - have been implemented in the PHSD and thus, we introduce a further step towards a consistent relativistic transport approach in the partonic sector.

In order to extract the Lagrange parameters  $\mu_B$  and  $T$  from the PHSD in heavy-ion collisions we developed a practical method (based on the expansion of thermodynamic quantities in terms of the 2nd order baryon number susceptibility) which allows to relate the energy density and baryon densities - calculated in each cell in space-time during heavy-ion collisions - to the DQPM EoS (practically identical to lQCD at small  $\mu_B$ ).

Finally, we will search for traces of the  $\mu_B$  dependence in the QGP dynamics in "bulk" observables from relativistic heavy-ion collisions such as rapidity distributions and  $p_T$  spectra using the extended PHSD approach as a working "tool".

This paper is organized as follows: In Section II we will provide a brief reminder of the DQPM and its ingredients as well as its results for the partonic equation of state. Section III will be devoted to the calculation of the partonic differential cross sections as a function of  $T$  and  $\mu_B$  employing the effective propagators and couplings from the DQPM. In Section IV we will use these cross sections to evaluate partonic scattering rates for fixed  $T$  and  $\mu_B$  as well as compute transport coefficients in Section V like the shear viscosity  $\eta$  in comparison to calculations from lQCD at  $\mu_B = 0$ . Section VI is devoted to the extraction of the local  $T$  and  $\mu_B$  in the actual transport approach and characteristic results will be presented for central collisions of Pb+Pb at  $\sqrt{s_{NN}} = 17.3$  and Au+Au 200 GeV. In Section VII we will compare the results of the novel transport approach PHSD5.0 to those of PHSD4.0 and experimental data for central heavy-ion collisions from AGS to RHIC energies. Furthermore, we explore the sensitivity of rapidity distributions and transverse momentum spectra to the partonic scattering in asymmetric C+Au collisions at the top SPS and RHIC energies. A summary of our study will be presented in Section VIII while technical details in the calculation of the matrix elements and differential cross sections are shifted to the [Appendices](#).

## II. REMINDER OF THE DQPM AND ITS INGREDIENTS

Early concepts of the Quark-Gluon-Plasma (QGP) were guided by the idea of a weakly interacting system of massless partons which might be described by perturbative QCD (pQCD). However, experimental observations at RHIC indicated that the new medium created in ultrarelativistic Au+Au collisions is interacting more strongly than hadronic matter. It is presently widely accepted that this medium is a strongly interacting system of partons as extracted experimentally from the strong radial expansion and the scaling of the elliptic flow  $v_2(p_T)$  of mesons and baryons with the number of constituent quarks and antiquarks [65]. At vanishing chemical potential  $\mu_B$  the QCD problem can be addressed at zero and finite temperature by lattice QCD calculations on a 3+1 dimensional torus with a suitable discretization of the QCD action on the euclidean lattice. These calculations so far have provided valuable information on the QCD equation of state, chiral symmetry restoration and various correlators that can be attributed/related to transport coefficients. Due to the Fermion 'sign'-problem lQCD calculations at finite  $\mu_B$  are presently not robust and one has to rely on nonperturbative - but effective - models to obtain information in the  $(T, \mu_B)$  plane or for systems out-of-equilibrium.

### A. Quasiparticle properties

As mentioned above in the KB theory the field quanta are described in terms of dressed propagators with complex self-energies [26]. Whereas the real part of the self-energies can be related to mean-field potentials (of Lorentz scalar, vector or tensor type), the imaginary parts provide information about the lifetime and/or reaction rates of time-like 'particles'. The determination/extraction of complex self-energies for the partonic degrees-of-freedom can be performed within the DQPM by fitting lattice QCD calculations in thermal equilibrium.

The basic ideas of the DQPM are as follows:

- i) introduce an ansatz (with a few parameters) for the  $(T$  and  $\mu_B)$ -dependence of masses and widths of the dynamical quasiparticles (quarks, antiquarks and gluons) to define the self-energies;
- ii) define the form of propagators for strongly interacting massive partons;
- iii) evaluate the QGP thermodynamics in equilibrium using the Kadanoff-Baym (KB) theory and calculate (in the 2PI approximation) the entropy density  $s$  and other thermodynamic quantities such as the pressure  $P$  and energy density
- iv) compare the DQPM results with the lQCD ones at zero and finite  $\mu_B$  and  $T$  and fix the initial parameters to obtain the best reproduction of the lQCD thermodynamics.

This defines the properties of the quasiparticles, their propagators and couplings.

We recall the main ingredients of the DQPM:

1) The DQPM postulates retarded propagators of the quark and gluon degrees-of-freedom (for the QGP in equilibrium) in the form

$$G^R(\omega, \mathbf{p}) = \frac{1}{\omega^2 - \mathbf{p}^2 - M^2 + 2i\gamma\omega} \quad (1)$$

using  $\omega = p_0$  for energy.

2) The coupling (squared)  $g^2$ , which is the essential quantity in the DQPM defining the strength of the interaction and enters the definition of the DQPM thermal masses and widths, is extracted from lQCD. In our previous studies [66–68] we used an ansatz for the  $(T, \mu_B)$ -dependence of the coupling  $g^2 = \alpha_s/(4\pi)$  and extracted the 2 parameters - entering the parametrization of  $g^2$  - from a global fit to the lQCD thermodynamics. Furthermore,  $g^2$  was also compared to quenched QCD results on  $\alpha_s(T)$  at  $\mu_B = 0$  for the pure glue case ( $N_f = 0$ ) from Ref. [69].

Here we follow alternatively a procedure similar to Refs. [63, 64] to determine the effective coupling (squared)  $g^2$  as a function of temperature  $T$ , i.e. the coupling is defined at  $\mu_B = 0$  by a parametrization of the entropy density from lattice QCD in the following way:

$$g^2(s/s_{SB}) = d((s/s_{SB})^e - 1)^f \quad (2)$$

with the Stefan-Boltzmann entropy density  $s_{SB}^{QCD} = 19/9\pi^2 T^3$  and the parameters  $d=169.934$ ,  $e=-0.178434$  and  $f=1.14631$ . In the following, we use a parametrization of the entropy density at  $\mu_B = 0$  calculated by lQCD from Refs. [70, 71] to determine the DQPM coupling constant as a function of temperature.

The extension to finite  $\mu_B$  can be worked out in different scenarios. First of all, an expansion of the grand-canonical potential, i.e. the negative pressure  $P$ , in terms of  $\mu_B/T$  can be performed and the expansion coefficients can be calculated by lQCD [72, 73]. This provides a solid framework for small and moderate  $\mu_B$ . Alternatively, Maxwell relations can be employed to extract the thermodynamic potential at finite  $\mu_B$  starting from the information given by lQCD at  $\mu_B = 0$  [74]. Both methods give almost the same results up to  $\mu_B \approx 450$  MeV [74]. For practical purposes the explicit results can be fitted by a scaling ansatz [64] which works up to  $\mu_B \approx 450$  MeV and suggests that the phase transition to the QGP is a crossover up to such baryon chemical potentials. We mention that the experimental studies of the STAR Collaboration within the BES program down to bombarding energies of  $\sqrt{s_{NN}} = 7.7$  GeV - corresponding to  $\mu_B \approx 450$  MeV - did not indicate any critical point in the QCD phase diagram [75] so far.

To obtain the coupling constant at finite baryon chemical potential  $\mu_B$ , the scaling hypothesis assumes that  $g^2$  is a function of the ratio of the effective temperature  $T^* = \sqrt{T^2 + \mu_q^2/\pi^2}$  and the  $\mu_B$ -dependent critical temperature  $T_c(\mu_B)$  as:

$$g^2(T/T_c, \mu_B) = g^2\left(\frac{T^*}{T_c(\mu_B)}, \mu_B = 0\right) \quad (3)$$

with  $\mu_B = 3\mu_q$ ,  $T_c(\mu_B) = T_c\sqrt{1 - \alpha\mu_B^2}$ , where  $T_c$  is the critical temperature at vanishing chemical potential ( $\approx 0.158$  GeV) and  $\alpha = 0.974$  GeV<sup>-2</sup>.

In Fig. 1 the DQPM running coupling  $\alpha_s = g^2(T, \mu_B)/(4\pi)$  is displayed as a function of the scaled temperature  $T/T_c(\mu_B)$  for different values of the baryon chemical potential  $\mu_B$ . We find that with increasing  $\mu_B$  the effective coupling drops in the vicinity of the critical temperature  $T_c(\mu_B)$ . This drop is rather moderate up to  $\mu_B = 0.4$  GeV (adequate for central Au+Au collisions at 30 A GeV) but becomes significant for  $\mu_B = 0.6$  GeV (roughly adequate for central Au+Au collisions at 10 A GeV). A comparison to the lattice results for quenched QCD from Ref. [69] - scaled by  $T_c \approx 270$  MeV - shows that the DQPM coupling qualitatively matches the lattice results but is slightly larger for lower  $\mu_B$ . We note, however, that this comparison should be taken only for orientation since the DQPM coupling corresponds to unquenched QCD with three light flavors ( $N_f = 2+1$ ) whereas the lattice results are for quenched QCD ( $N_f = 0$ ). Note that - since the running coupling (squared)  $g^2 \sim (11N_c - 2N_f)^{-1}$  ( $N_c = 3$ ) - the coupling is larger for a finite number of flavors  $N_f$  compared to  $N_f = 0$ .

With the coupling  $g^2$  fixed from lQCD one can now specify the dynamical quasiparticle mass (for gluons and quarks) which is assumed to be given by the HTL thermal mass in the asymptotic high-momentum regime, i.e. for gluons by

$$M_g^2(T, \mu_B) = \frac{g^2(T, \mu_B)}{6} \left( \left( N_c + \frac{1}{2}N_f \right) T^2 + \frac{N_c}{2} \sum_q \frac{\mu_q^2}{\pi^2} \right), \quad (4)$$

and for quarks (antiquarks) by

$$M_{q(\bar{q})}^2(T, \mu_B) = \frac{N_c^2 - 1}{8N_c} g^2(T, \mu_B) \left( T^2 + \frac{\mu_q^2}{\pi^2} \right) \quad (5)$$

where  $N_c = 3$  stands for the number of colors while  $N_f (= 3)$  denotes the number of flavors. The dynamical masses (5) in the QGP are large compared to the bare masses of the light ( $u, d$ ) quarks and adopted in the form (5) for the ( $u, d$ ) quarks. The strange quark has a larger bare mass which also enters to some extent the



dynamical mass  $M_s(T)$ . This essentially suppresses the channel  $g \rightarrow s + \bar{s}$  relative to the channel  $g \rightarrow u + \bar{u}$  or  $d + \bar{d}$  and controls the strangeness ratio in the QGP. Empirically we have used  $M_s(T, \mu_B) = M_u(T, \mu_B) + \Delta M = M_d(T, \mu_B) + \Delta M$  where  $\Delta M = 30$  MeV, which has been fixed once in comparison to experimental data for the  $K^+/\pi^+$  ratio in central Au+Au collisions at  $\sqrt{s_{NN}} = 200$  GeV. Furthermore, the effective quarks, antiquarks and gluons in the DQPM have finite widths, which are adopted in the form

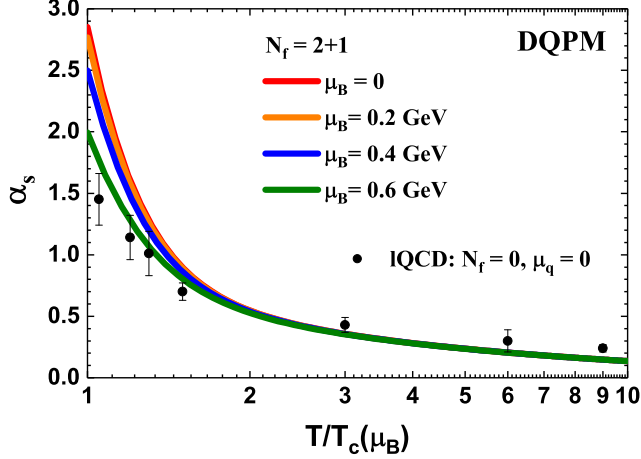


FIG. 1. (Color online) The DQPM running coupling  $\alpha_s = g^2(T, \mu_B)/(4\pi)$  (for  $N_f = 2+1$ ) as a function of the scaled temperature  $T/T_c(\mu_B)$  for different values of the baryon chemical potential  $\mu_B$ . The lattice results for quenched QCD (for  $N_f = 0$ ) are taken from Ref. [69] and scaled by the critical temperature  $T_c \approx 270$  MeV.

$$\gamma_g(T, \mu_B) = \frac{1}{3} N_c \frac{g^2(T, \mu_B) T}{8\pi} \ln \left( \frac{2c}{g^2(T, \mu_B)} + 1 \right), \quad (6)$$

$$\gamma_{q(\bar{q})}(T, \mu_B) = \frac{1}{3} \frac{N_c^2 - 1}{2N_c} \frac{g^2(T, \mu_B) T}{8\pi} \ln \left( \frac{2c}{g^2(T, \mu_B)} + 1 \right), \quad (7)$$

where  $c = 14.4$  is related to a magnetic cut-off, which is an additional parameter of the DQPM. Furthermore, we assume that the width of the strange quark is the same as that for the light ( $u, d$ ) quarks.

The physical processes contributing to the width  $\gamma_g$  are both  $gg \leftrightarrow gg$ ,  $gq \leftrightarrow gq$  scattering as well as splitting and fusion reactions  $gg \leftrightarrow g$ ,  $gg \leftrightarrow ggg$ ,  $ggg \leftrightarrow gggg$  or  $g \leftrightarrow q\bar{q}$  etc. On the fermion side elastic fermion-fermion scattering  $pp \leftrightarrow pp$ , where  $p$  stands for a quark  $q$  or antiquark  $\bar{q}$ , fermion-gluon scattering  $pg \leftrightarrow pg$ , gluon bremsstrahlung  $pp \leftrightarrow pp + g$  or quark-antiquark fusion  $q\bar{q} \leftrightarrow g$  etc. emerge. Note, however, that the explicit form of (6) is derived for hard two-body scatterings only. Furthermore, the widths  $\gamma_{q(\bar{q})}(T)$  and  $\gamma_g(T)$  provide only information on the total interaction rates and not on the

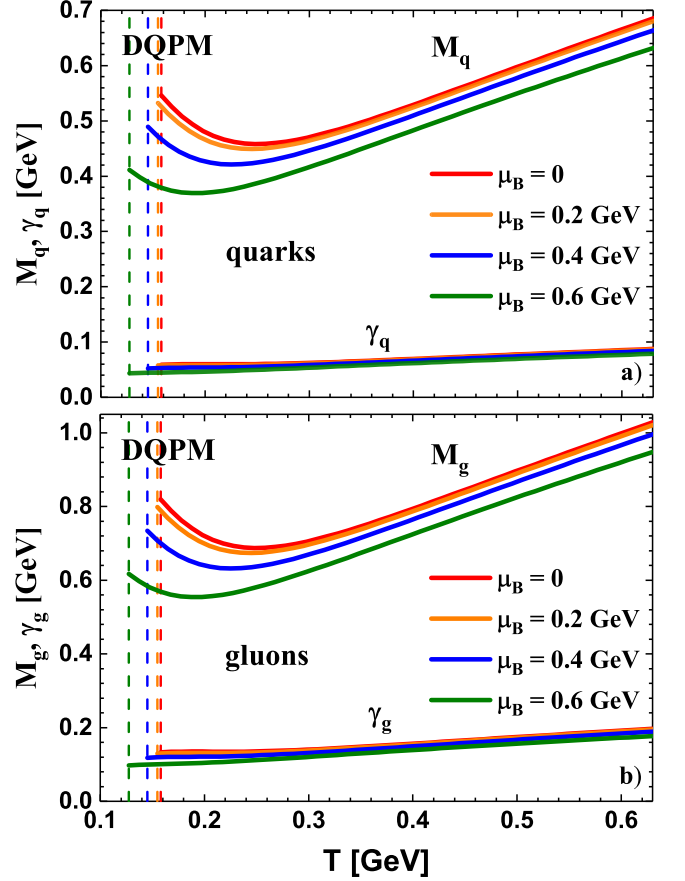


FIG. 2. (Color online) The effective quark (a) and gluon (b) masses  $M$  and widths  $\gamma$  (from the parametrizations (6) and (7)) as a function of the temperature  $T$  for different  $\mu_B$ . The vertical dashed lines correspond to the DQPM  $\mu_B$  dependent critical temperature  $T_c(\mu_B)$ .

individual differential cross sections. The computation of these cross sections will be carried out here in leading order on the basis of the propagators (1) and coupling (2)-(3) in Section III which in turn will allow to recalculate the widths (6) and (7) and explore the validity of the quasiparticle limit in the time-like sector.

## B. Spectral functions

In line with the propagator (1) the parton spectral functions (or imaginary parts of the propagator  $\rho = -2 \text{Im } G^R$ ) are no longer  $\delta$ -functions in the invariant mass squared but given by

$$\begin{aligned} \rho_j(\omega, \mathbf{p}) &= \frac{\gamma_j}{\tilde{E}_j} \left( \frac{1}{(\omega - \tilde{E}_j)^2 + \gamma_j^2} - \frac{1}{(\omega + \tilde{E}_j)^2 + \gamma_j^2} \right) \\ &\equiv \frac{4\omega\gamma_j}{(\omega^2 - \mathbf{p}^2 - M_j^2)^2 + 4\gamma_j^2\omega^2} \end{aligned} \quad (8)$$

separately for quarks, antiquarks and gluons ( $j = q, \bar{q}, g$ ).

Here  $\tilde{E}_j^2(\mathbf{p}) = \mathbf{p}^2 + M_j^2 - \gamma_j^2$ , where the widths  $\gamma_j$  and masses  $M_j$  from the DQPM have been described above. The spectral function (8) is antisymmetric in  $\omega$  and normalized as [76]

$$\int_{-\infty}^{\infty} \frac{d\omega}{2\pi} \omega \rho_j(\omega, \mathbf{p}) = \int_0^{\infty} \frac{d\omega}{2\pi} 2\omega \rho_j(\omega, \mathbf{p}) = 1 \quad (9)$$

as mandatory for quantum field theory.

The actual quark mass  $M_q$  and width  $\gamma_q$  – employed as input in the previous PHSD calculations – as well as the gluon mass  $M_g$  and width  $\gamma_g$  are depicted in Fig. 2 as a function of  $T/T_c$  and show an ‘infrared enhancement’ close to  $T_c$ . For  $\mu_q = \mu_B/3 = 0$  the DQPM gives

$$M_q = \frac{2}{3}M_g, \quad \gamma_q = \frac{4}{9}\gamma_g. \quad (10)$$

### C. Thermodynamics within the DQPM

With the quasiparticle properties (or propagators) chosen as described above, one can evaluate the entropy density  $s(T, \mu_B)$ , the pressure  $P(T, \mu_B)$  and energy density  $\epsilon(T, \mu_B)$  in a straight forward manner by starting with the entropy density and number density in the propagator representation from Baym [36, 77],

$$s^{dqp} = \quad (11)$$

$$\begin{aligned} & - \int \frac{d\omega}{2\pi} \frac{d^3p}{(2\pi)^3} \left[ d_g \frac{\partial n_B}{\partial T} (\text{Im}(\ln -\Delta^{-1}) + \text{Im} \Pi \text{Re} \Delta) \right. \\ & + \sum_{q=u,d,s} d_q \frac{\partial n_F(\omega - \mu_q)}{\partial T} (\text{Im}(\ln -S_q^{-1}) + \text{Im} \Sigma_q \text{Re} S_q) \\ & \left. + \sum_{\bar{q}=\bar{u},\bar{d},\bar{s}} d_{\bar{q}} \frac{\partial n_F(\omega + \mu_q)}{\partial T} (\text{Im}(\ln -S_{\bar{q}}^{-1}) + \text{Im} \Sigma_{\bar{q}} \text{Re} S_{\bar{q}}) \right] \end{aligned}$$

$$\begin{aligned} n^{dqp} = & - \int \frac{d\omega}{2\pi} \frac{d^3p}{(2\pi)^3} \\ & \left[ \sum_{q=u,d,s} d_q \frac{\partial n_F(\omega - \mu_q)}{\partial \mu_q} (\text{Im}(\ln -S_q^{-1}) + \text{Im} \Sigma_q \text{Re} S_q) \right. \\ & \left. + \sum_{\bar{q}=\bar{u},\bar{d},\bar{s}} d_{\bar{q}} \frac{\partial n_F(\omega + \mu_q)}{\partial \mu_q} (\text{Im}(\ln -S_{\bar{q}}^{-1}) + \text{Im} \Sigma_{\bar{q}} \text{Re} S_{\bar{q}}) \right] \end{aligned} \quad (12)$$

where  $n_B(\omega) = (\exp(\omega/T) - 1)^{-1}$  and  $n_F(\omega - \mu_q) = (\exp((\omega - \mu_q)/T) + 1)^{-1}$  denote the Bose-Einstein and Fermi-Dirac distribution functions, respectively, while  $\Delta = (p^2 - \Pi)^{-1}$ ,  $S_q = (p^2 - \Sigma_q)^{-1}$  and  $S_{\bar{q}} = (p^2 - \Sigma_{\bar{q}})^{-1}$  stand for the full (scalar) quasiparticle propagators of gluons  $g$ , quarks  $q$  and antiquarks  $\bar{q}$ . In Eq. (11-12)

$\Pi$  and  $\Sigma = \Sigma_q \approx \Sigma_{\bar{q}}$  denote the (retarded) quasiparticle self-energies. Furthermore, the number of transverse gluonic degrees-of-freedom is  $d_g = 2 \times (N_c^2 - 1)$  while for the fermion degrees-of-freedom we use  $d_q = 2 \times N_c$  and  $d_{\bar{q}} = 2 \times N_c$ .

In principle,  $\Pi$  as well as  $\Delta$  are Lorentz tensors and should be evaluated in a nonperturbative framework. The DQPM treats these degrees-of-freedom as independent scalar fields (for each color and spin projection) with scalar self-energies which are assumed to be identical for quarks and antiquarks. This is expected to hold well for the entropy and number density. Note that one has to treat quarks and antiquarks separately in Eqs. (11)-(12) as their abundance differs at finite quark chemical potential  $\mu_q = \mu_B/3$ .

With the choice (8) the complex self-energies  $\Pi = M_g^2 - 2i\omega\gamma_g$  and  $\Sigma_q = M_q^2 - 2i\omega\gamma_q$  are fully defined via (4), (5), (6), (7). Note that the retarded propagator (1) resembles the propagator of a damped harmonic oscillator (with an additional  $\mathbf{p}^2$ ) and preserves microcausality also for  $\gamma > M$  [78], i.e. in case of overdamped motion. Although the ‘Ansatz’ for the parton propagators is not QCD it has been shown that a variety of QCD observables on the lattice are compatible with this choice [55].

In case the real and imaginary parts of the propagators  $\Delta$  and  $S$  are fixed, the entropy density (11) and number density (12) can be evaluated numerically. As we deal with a grand-canonical ensemble the Maxwell relations give,

$$s = \frac{\partial P}{\partial T} ; \quad n_B = \frac{\partial P}{\partial \mu_B}, \quad (13)$$

such that the pressure can be obtained by integration of the entropy density  $s$  over  $T$  and of the baryon density  $n_B$  over  $\mu_B$  as:

$$\begin{aligned} P(T, \mu_B) = & P(T_0, 0) + \int_{T_0}^T s(T', 0) dT' \\ & + \int_0^{\mu_B} n_B(T, \mu'_B) d\mu'_B \end{aligned} \quad (14)$$

where one identifies the ‘full’ entropy density  $s$  and baryon density  $n_B$  with the quasiparticle entropy density  $s^{dqp}$  (11) and baryon density  $n_B = n^{dqp}/3$  (12). The starting point  $T_0$  for the integration in  $T$  is chosen between  $0.1 < T < 0.15$  GeV where the entropy density is taken in accordance to the lattice QCD results from Ref. [71] in the hadronic sector.

The energy density  $\epsilon$  then follows from the thermodynamical relation

$$\epsilon = Ts - P + \mu_B n_B \quad (15)$$

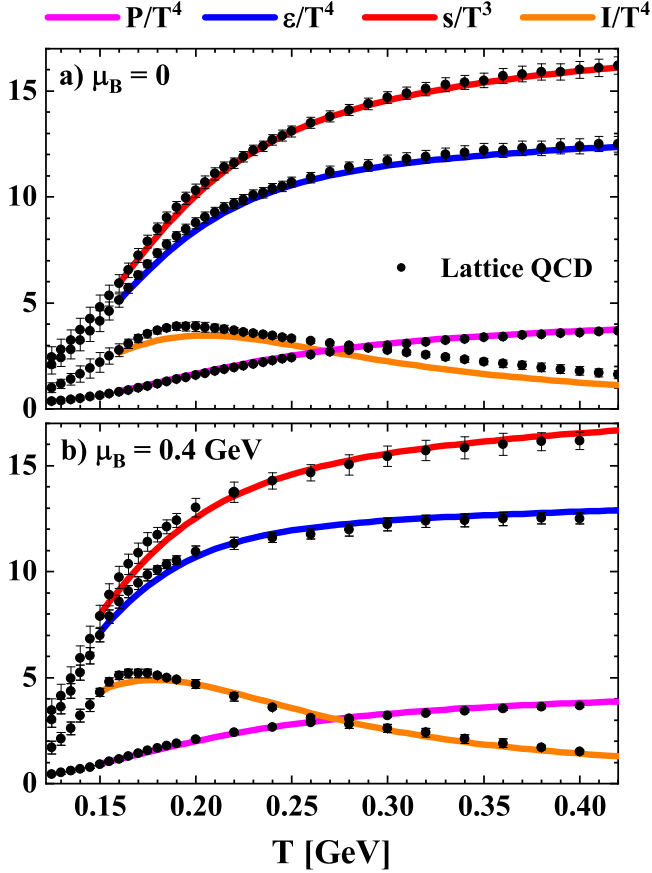


FIG. 3. (Color online) The scaled pressure  $P(T)/T^4$  (pink line), entropy density  $s(T)/T^3$  (red line), scaled energy density  $\epsilon(T)/T^4$  (blue line), and interaction measure (16) (orange line), from the DQPM in comparison to the lQCD results from Refs. [70, 71] (full dots) for  $\mu_B = 0$  (a) and  $\mu_B = 400$  MeV (b).

and thus is also fixed by the entropy  $s(T, \mu_B)$  and baryon density  $n_B(T, \mu_B)$  as well as the interaction measure

$$I := \epsilon - 3P = Ts - 4P + \mu_B n_B \quad (16)$$

that vanishes for massless and noninteracting degrees-of-freedom at  $\mu_B = 0$ .

A direct comparison of the resulting entropy density  $s(T)$  (11), pressure  $P(T)$  (14), energy density  $\epsilon(T)$  (15) and interaction measure (16) from the DQPM with lQCD results from the BMW group [70, 71] at  $\mu_B = 0$  (a) and  $\mu_B = 400$  MeV (b) is presented in Fig. 3. The dimensionless results  $s/T^3$ ,  $P/T^4$  and  $\epsilon/T^4$ , are shown to demonstrate the scaling with temperature. The agreement is sufficiently good for the entropy and energy density as well as for the pressure. A satisfactory agreement also holds for the dimensionless 'interaction measure', i.e.  $(\epsilon - 3P)/T^4$  (cf. orange line in Fig. 3).

### III. DIFFERENTIAL CROSS SECTIONS FOR PARTONIC INTERACTIONS

#### A. Definitions

##### 1. On-shell case

The differential cross section for a  $2 \rightarrow 2$  process of on-shell particles ( $1 + 2 \rightarrow 3 + 4$ ) is given by:

$$d\sigma^{\text{on}} = \frac{d^3 p_3}{(2\pi)^3 2E_3} \frac{d^3 p_4}{(2\pi)^3 2E_4} \times (2\pi)^4 \delta^{(4)}(p_1 + p_2 - p_3 - p_4) \frac{|\bar{\mathcal{M}}|^2}{F}, \quad (17)$$

where the flux is defined by  $F = v_{\text{rel}} 2E_1 2E_2$  with the definition  $v_{\text{rel}} = |\vec{v}_1 - \vec{v}_2|$ , and the on-shell energies for the particle are defined as  $E_j = \sqrt{\mathbf{p}_j^2 + M_j^2}$ .  $|\bar{\mathcal{M}}|^2$  denotes the matrix element squared averaged over the color and spin of the incoming particles, and summed over those of the final particles. We want to evaluate the cross section in the rest frame of the heat bath where the Fermi-Dirac or Bose-Einstein functions describe the particle distributions. The only factor in Eq. (17), which is not Lorentz invariant, is the flux factor  $F$  while the other factors, the Lorentz Invariant Phase Space (LIPS), the matrix element  $|\bar{\mathcal{M}}|^2$  and the delta function for energy-momentum conservation, are invariant. This implies that the cross section can be calculated in any frame, but the flux factor has to be correctly taken into account according to the actual frame of interest.

The cross section is usually evaluated in the center of mass (CM) frame of the collision for simplicity. In this case the momenta of the colliding particles obey  $\mathbf{p}_1 + \mathbf{p}_2 = \mathbf{p}_3 + \mathbf{p}_4 = \mathbf{p} = \vec{0}$ , and the notation  $|\mathbf{p}_1| = |\mathbf{p}_2| = p_i$  and  $|\mathbf{p}_3| = |\mathbf{p}_4| = p_f$  is used. The flux factor becomes  $F^{\text{CM}} = 4p_i \sqrt{s}$  and, after simplification, Eq. (17) reads:

$$d\sigma_{\text{on}}^{\text{CM}} = \frac{p_f d\Omega}{16\pi^2 \sqrt{s}} \frac{|\bar{\mathcal{M}}|^2}{F^{\text{CM}}} = \frac{d\Omega}{64\pi^2 s} \frac{p_f}{p_i} |\bar{\mathcal{M}}|^2, \quad (18)$$

where  $s$  is the Mandelstam variable and  $d\Omega$  is the differential solid angle corresponding to one of the final particle. The momenta of the initial ( $i$ ) and final particles ( $f$ ) in the CM frame is found to be:

$$p_{i,f} = \frac{\sqrt{\left(s - (M_{i,f} + M'_{i,f})^2\right) \left(s - (M_{i,f} - M'_{i,f})^2\right)}}{2\sqrt{s}}, \quad (19)$$

with  $M_{i,f}$  and  $M'_{i,f}$  being the masses of the colliding partons. The total cross section is obtained by performing the integral in Eq. (18) over  $d\Omega$  as:

$$\sigma_{\text{on}}^{\text{CM}} = \frac{1}{32\pi s} \frac{p_f}{p_i} \int_{-1}^1 d\cos(\theta) |\bar{\mathcal{M}}|^2, \quad (20)$$

where  $\theta$  is the final polar angle of one of the final particle in the CM frame. In the CM frame, the collision is independent from the azimuthal angle  $\phi$  and the corresponding integration gives a factor  $2\pi$ .

## 2. Off-shell case

In the off-shell case, the energy of the partons, as well their momenta, are independent degrees of freedom and a general definition of an 'off-shell cross section' is not possible due to the lack of asymptotically stable states. However, transition matrix elements for different incoming and outgoing 4-momenta can be well defined also off-shell. By transforming the Lorentz invariant phase space in Eq. (17), one can include the off-shell effects for the scattering of time-like particles - in case of a well defined incoming flux  $F = v_{\text{rel}} 2E_1 2E_2$  - by integrating over the energy of the final time-like particles as:

$$Fd\sigma^{\text{off}} = \frac{d^4 p_3}{(2\pi)^4} \frac{d^4 p_4}{(2\pi)^4} \tilde{\rho}_3(\omega_3, \mathbf{p}_3) \theta(\omega_3) \tilde{\rho}_4(\omega_4, \mathbf{p}_4) \theta(\omega_4) \times (2\pi)^4 \delta^{(4)}(p_1 + p_2 - p_3 - p_4) |\bar{\mathcal{M}}|^2 \quad (21)$$

with the renormalized time-like spectral functions

$$\tilde{\rho}_j(\omega_j, \mathbf{p}_j) = \frac{\rho(\omega_j, \mathbf{p}_j) \theta(p_j^2)}{\int_0^\infty \frac{d\omega_j}{(2\pi)} 2\omega_j \rho(\omega_j, \mathbf{p}_j) \theta(p_j^2)}, \quad (22)$$

where the spectral function  $\rho_i$  in (22) - corresponding to the parton type  $i$  - is taken from Eq. (8). The final parton masses are defined as  $m_i^2 = p_i^2 = \omega_i^2 - \mathbf{p}_i^2$  where  $p_i$  is the 4-momentum of particle  $i$ . One can verify that by replacing the spectral functions by their on-shell value:

$$\lim_{\gamma_j \rightarrow 0} \rho_j(\omega, \mathbf{p}) = 2\pi \delta(\omega^2 - \mathbf{p}^2 - M_j^2) \quad (23)$$

$$= \frac{\pi}{\omega} \left[ \delta(\omega - \sqrt{\mathbf{p}^2 + M_j^2}) + \delta(\omega + \sqrt{\mathbf{p}^2 + M_j^2}) \right],$$

the off-shell cross section leads to the on-shell one as defined in the previous subsection from Eq. (17).

We follow the same strategy as in the previous subsection and evaluate the differential "off-shell cross section" for time-like quanta in the center of mass system of the collision for convenience. By making use of the delta function in Eq. (21), one can integrate over  $d^4 p_4$  to obtain the total cross section in the CM frame by performing the integrations with the appropriate boundaries as:

$$F^{\text{CM}} \sigma_{\text{off}}^{\text{CM}} = \frac{1}{(2\pi)^3} \int_0^{\sqrt{s}/2} p_f^2 dp_f d\cos(\theta) \int_{p_f}^{\sqrt{s}-p_f} d\omega_3^{\text{CM}} \tilde{\rho}_3(\omega_3, \mathbf{p}_3) \tilde{\rho}_4(\omega_4, \mathbf{p}_4) |\bar{\mathcal{M}}|^2 \quad (24)$$

for  $F^{\text{CM}} = 4p_i^{\text{CM}} \sqrt{s}$ . Bear in mind that even if the calculation of the cross section is performed in the center of mass system, the energies and momenta entering the spectral functions (8) should be expressed in the heat bath frame by applying the appropriate Lorentz transformations.

We mention that one can simplify the off-shell energy integration by an integration over the final masses of the partons in the non-relativistic limit. The off-shell cross section from Eq. (21) then becomes [66]:

$$\sigma_{\text{off}}^{\text{BW}} = \int_0^{\sqrt{s}} dm_3 \int_0^{\sqrt{s}-m_3} dm_4 \rho^{\text{BW}}(m_3) \rho^{\text{BW}}(m_4) \int d\sigma_{\text{on}}^{\text{CM}}, \quad (25)$$

where the Breit-Wigner spectral function  $\rho^{\text{BW}}$  in Ref. [66] is obtained from Eq. (8) in the limit  $\omega \rightarrow m$ :

$$\rho_i^{\text{BW}}(m) = \frac{2}{\pi} \frac{2m^2 \gamma_i}{(m^2 - M_i^2)^2 + (2m\gamma_i)^2}. \quad (26)$$

This distribution fulfills the normalization  $\int_0^\infty dm \rho^{\text{BW}}(m) = 1$ .

## B. Partonic scattering

In the framework of the DQPM, quarks and gluons are massive with a finite lifetime associated to their interaction width. In order to calculate the matrix elements corresponding to a scattering of DQPM partons, the scalar propagator (1) has to be replaced by the following propagators - with full Lorentz structure - to describe a massive vector gluon and massive (spin 1/2) fermion with a finite width [66]:

$$\overset{\mu, a}{\text{oooooo}} \underset{q}{\text{oooooo}} \overset{\nu, b}{\text{oooooo}} = -i\delta_{ab} \frac{g^{\mu\nu} - q^\mu q^\nu / M_g^2}{q^2 - M_g^2 + 2i\gamma_g q_0}, \quad (27)$$

$$\overset{i}{\text{---}} \underset{q}{\text{---}} \overset{j}{\text{---}} = i\delta_{ij} \frac{\not{q} + M_q}{q^2 - M_q^2 + 2i\gamma_q q_0}, \quad (28)$$

where  $q$  is the 4-momentum of the exchanged particle. The delta functions ensure that the exchanged quark or gluon is connected with other parts of the diagram with



the same color ( $a, b$  for the gluon and  $i, j$  for the quark). The invariant matrix element (squared)  $|\mathcal{M}|^2$ , entering the differential cross section in Eqs. (17)-(21), is calculated in leading order, and is averaged over initial - and summed over final - spin and colors. In the following, we employ a degeneracy factor for spin and color of  $d_q = 2 \times N_c = 6$  for quarks, and  $d_g = 2 \times (N_c^2 - 1) = 16$  for

gluons in consistency with Eqs. (11)-(12). Each matrix element can be decomposed into several channels known as  $t$ -,  $u$ -,  $s$ -channels for quark-quark ( $qq'$ ) and quark-gluon ( $qg$ ) scatterings, as well as a 4-point interaction for the case of gluon-gluon ( $gg$ ) scattering. For details we refer the reader to the Appendices (A,B,C) and continue with the actual results.

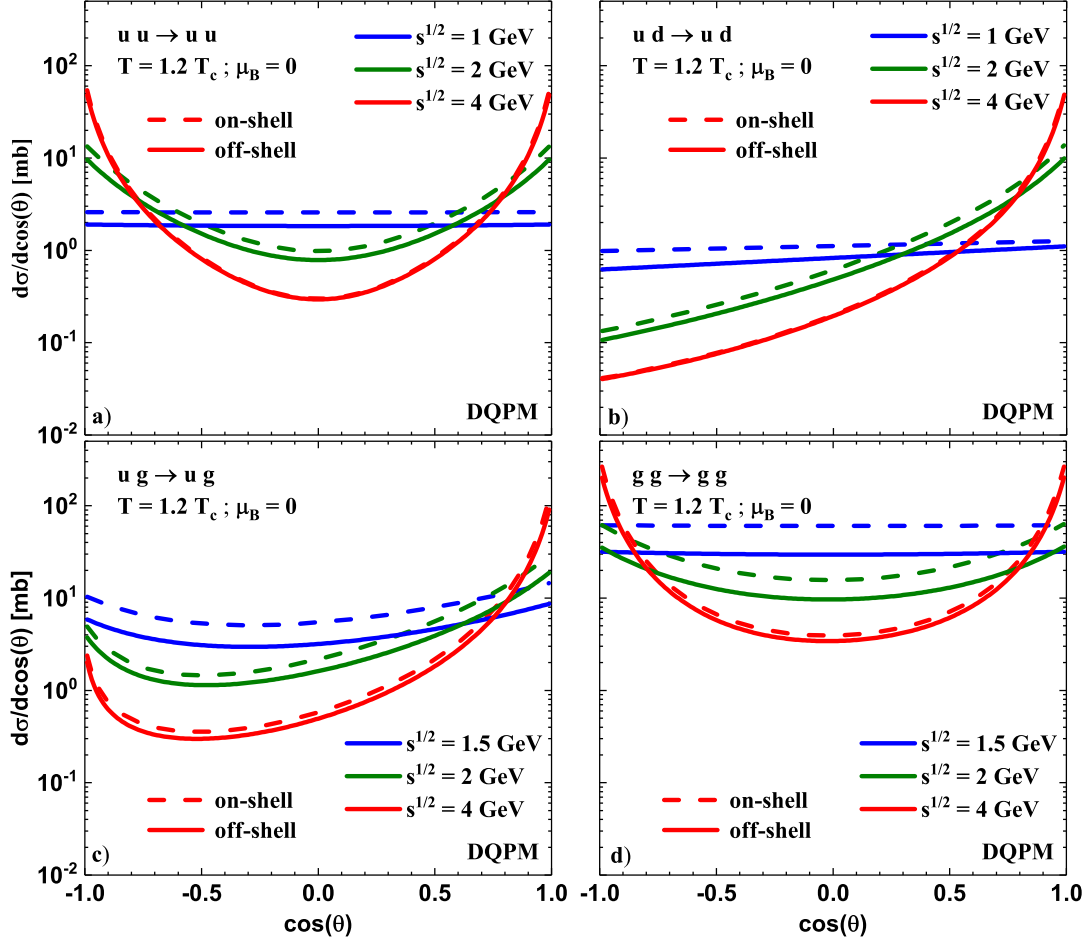


FIG. 4. (Color online) Elastic differential cross sections between different partons for the on-shell case (dashed lines) from Eq. (18) and the "off-shell case" (solid lines) evaluated in the center of mass of the collision system as a function of the angle  $\cos(\theta)$  between the initial and final momentum of one of the partons for  $T = 1.2T_c$  and  $\mu_B = 0$ . The initial masses of the colliding partons are taken as the pole masses from Eqs. (4)-(5). The different lines correspond to different collision energies  $\sqrt{s}$  from 1 to 4 GeV (see legend).

In Fig. 4 we show the differential cross sections between different partons for the on-shell case (dashed lines) from Eq. (18) and the "off-shell case" (solid lines) evaluated in the center of mass of the collision system as a function of the collision energy  $\sqrt{s}$ . In these examples the initial masses of the colliding partons are taken as the pole masses from Eqs. (4)-(5) to allow for a comparison between on-shell and off-shell scattering, i.e. for the same initial states. In all cases ( $uu \rightarrow uu$  (a),  $ud \rightarrow ud$  (b),

$ug \rightarrow ug$  (c),  $gg \rightarrow gg$  (d)) the cross sections are almost isotropic at  $\sqrt{s} \approx 1$  GeV and increase in anisotropy with increasing  $\sqrt{s}$ . Furthermore, the on-shell case (dashed lines) gives slightly larger cross sections than the off-shell case (solid lines) which will be discussed below.

Fig. 5 (a) displays the angle integrated cross section for  $uu \rightarrow uu$  scattering as a function of  $\sqrt{s}$  for temperatures of  $T = 1.2T_c$  (blue),  $T = 2T_c$  (green), and  $T = 3T_c$  (red) for the on-shell (dashed lines) and off-shell (solid lines)

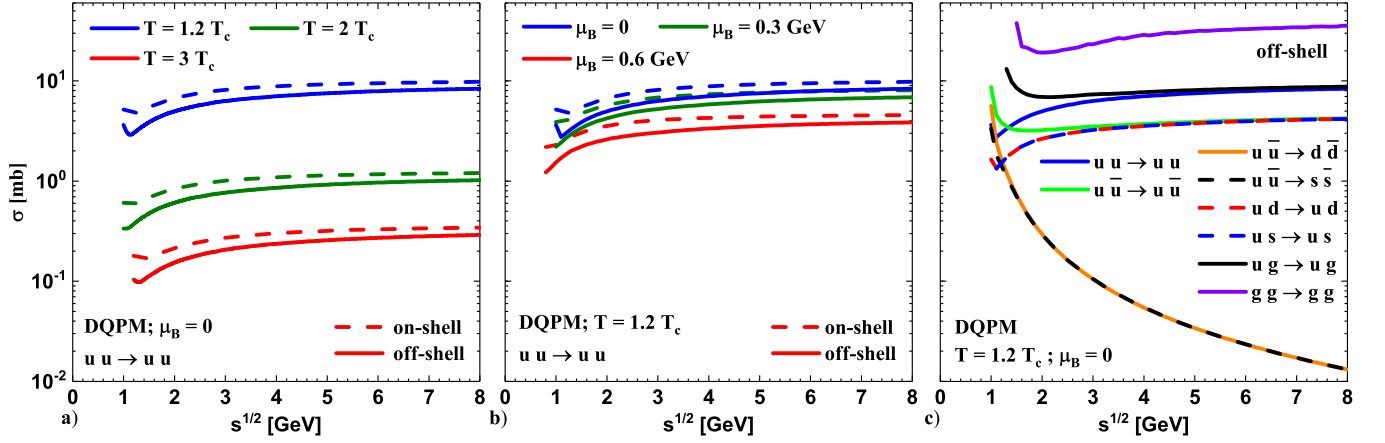


FIG. 5. (Color online) Cross sections between different partons for the on-shell case (dashed lines) from Eq. (20) and the "off-shell case" (solid lines) from Eq. (24) evaluated in the center of mass of the collision system as a function of the collision energy  $\sqrt{s}$  (see text for a detailed description). The initial masses of the colliding partons are taken as the pole masses from Eqs. (4)-(5).

cases at  $\mu_B = 0$ . Again the initial masses of the colliding partons are taken as the pole masses from Eqs. (4)-(5) to obtain the same initial flux  $F$ . At all temperatures  $T$  the cross section does not change very much with collision energy  $\sqrt{s}$  and the difference between the on-shell and off-shell case decreases with increasing  $\sqrt{s}$ . The explicit dependence of the  $uu \rightarrow uu$  cross section on the chemical potential is shown in Fig. 5 (b) for  $\mu_B = 0$  (blue),  $\mu_B = 0.3$  GeV (green) and  $\mu_B = 0.6$  GeV (red) at  $T = 1.2T_c$  for the on-shell (dashed lines) and off-shell (solid lines) cases. While the dependencies on  $\sqrt{s}$  are similar we find a decrease of the cross section with increasing chemical potential  $\mu_B$  which can be traced back to a decreasing coupling with  $\mu_B$  at fixed temperature  $T$  (see Fig. 1). Fig. 5 (c), furthermore, shows the dependence of all cross sections calculated on the collision energy  $\sqrt{s}$  in the off-shell case for  $T = 1.2T_c$  and  $\mu_B = 0$ . While most of the channels do not change drastically with  $\sqrt{s}$  - except for thresholds - the flavor changing processes  $u\bar{u} \rightarrow d\bar{d}$  and  $u\bar{u} \rightarrow s\bar{s}$  drop fast with increasing energy.

With all differential partonic cross sections fixed as a function of  $T$  and  $\mu_B$  (above the phase boundary) we can now continue with transport properties of the hot QGP as a function of  $T$  and  $\mu_B$  employing the partonic energy-momentum distributions from the DQPM.

#### IV. COLLISIONAL WIDTHS OF THE HOT AND DENSE QGP

##### 1. On-shell case

In the on-shell case all energies of the particles are taken to be  $E^2 = \mathbf{p}^2 + M^2$  where  $M$  is the pole mass. The on-shell interaction rate for the corresponding parton is given by [34, 79, 80]:

$$\begin{aligned} \Gamma_i^{\text{on}}(\mathbf{p}_i, T, \mu_q) &= \frac{1}{2E_i} \sum_{j=q,\bar{q},g} \int \frac{d^3p_j}{(2\pi)^3 2E_j} d_j f_j(E_j, T, \mu_q) \\ &\quad \times \int \frac{d^3p_3}{(2\pi)^3 2E_3} \int \frac{d^3p_4}{(2\pi)^3 2E_4} (1 \pm f_3)(1 \pm f_4) \\ &\quad \times |\bar{\mathcal{M}}|^2(p_i, p_j, p_3, p_4) (2\pi)^4 \delta^{(4)}(p_i + p_j - p_3 - p_4) \\ &= \sum_{j=q,\bar{q},g} \int \frac{d^3p_j}{(2\pi)^3} d_j f_j v_{\text{rel}} \int d\sigma_{ij \rightarrow 34}^{\text{on}} (1 \pm f_3)(1 \pm f_4), \end{aligned} \quad (29)$$

where  $d_j$  is the degeneracy factor for spin and color (for quarks  $d_q = 2 \times N_c$  and for gluons  $d_g = 2 \times (N_c^2 - 1)$ ), and with the shorthand notation  $f_j = f_j(E_j, T, \mu_q)$  for the distribution functions. In Eq. (29) and in all this section, the notation  $\sum_{j=q,\bar{q},g}$  includes the contribution from all possible partons which in our case are the gluons and the (anti-)quarks of three different flavors ( $u, d, s$ ). The Pauli-blocking (-) and Bose-enhancement (+) factors account for the available density of final states. Note that here all quantities have to be expressed in the rest frame of the heat bath, implying that the on-shell cross section  $d\sigma^{\text{on}}$  from Eq. (18) has to be modified according to the different fluxes:

$$F^{\text{HB}} \sigma^{\text{HB}} = \sigma^{\text{CM}} F^{\text{CM}}, \quad (30)$$

where the quantities denoted by HB are expressed in the rest frame of the heat bath and CM in the center of mass frame of the collision.

To evaluate the average width of the partons  $i$ , we finally have to average its interaction rate (29) over its

momentum distribution,

$$\Gamma_i^{\text{on}}(T, \mu_q) = \frac{d_i}{n_i^{\text{on}}(T, \mu_q)} \int \frac{d^3 p_i}{(2\pi)^3} f_i(E_i, T, \mu_q) \times \Gamma_i^{\text{on}}(\mathbf{p}_i, T, \mu_q) \quad (31)$$

with the on-shell density of partons  $i$  at  $T$  and  $\mu_q$  given by

$$n_i^{\text{on}}(T, \mu_q) = d_i \int \frac{d^3 p_i}{(2\pi)^3} f_i(E_i, T, \mu_q). \quad (32)$$

## 2. Off-shell case

In order to obtain the width for the off-shell DQPM time-like partons, we have to calculate the interaction rate for the corresponding parton  $i$  with momentum  $\mathbf{p}_i$  due to collisions with time-like particles  $j$  leading to final time-like particles 3 and 4 by integrating additionally over all energies  $\omega_j$  in the time-like sector:

$$\begin{aligned} \Gamma_i^{\text{off}}(\mathbf{p}_i, T, \mu_q) &= \int_0^\infty \frac{d\omega_i}{(2\pi)} \tilde{\rho}_i \sum_{j=q,\bar{q},g} \int \frac{d^4 p_j}{(2\pi)^4} \theta(\omega_j) d_j \tilde{\rho}_j f_j \\ &\times \int \frac{d^4 p_3}{(2\pi)^4} \theta(\omega_3) \tilde{\rho}_3 \int \frac{d^4 p_4}{(2\pi)^4} \theta(\omega_4) \tilde{\rho}_4 (1 \pm f_3)(1 \pm f_4) \\ &\times |\bar{\mathcal{M}}|^2(p_i, p_j, p_3, p_4) (2\pi)^4 \delta^{(4)}(p_i + p_j - p_3 - p_4), \end{aligned} \quad (33)$$

where the shorthand notation (22) for the renormalized time-like spectral functions  $\tilde{\rho}_j(\omega_j, \mathbf{p}_j)$  has been used and  $f_j = f_j(\omega_j, T, \mu_q)$  for the distribution functions. We mention that the limit (33) discards damping processes between the time-like and space-like sector which are assumed to be subleading. To evaluate the average time-like width of the partons  $i$ , we finally have to average its interaction rate as:

$$\begin{aligned} \Gamma_i^{\text{off}}(T, \mu_q) &= \frac{d_i}{n_i^{\text{off}}(T, \mu_q)} \int \frac{d^4 p_i}{(2\pi)^4} \theta(\omega_i) \tilde{\rho}_i f_i(\omega_i, T, \mu_q) \\ &\times \sum_{j=q,\bar{q},g} \int \frac{d^4 p_j}{(2\pi)^4} \theta(\omega_j) d_j \tilde{\rho}_j f_j \\ &\times \int \frac{d^4 p_3}{(2\pi)^4} \theta(\omega_3) \tilde{\rho}_3 \int \frac{d^4 p_4}{(2\pi)^4} \theta(\omega_4) \tilde{\rho}_4 (1 \pm f_3)(1 \pm f_4) \\ &\times |\bar{\mathcal{M}}|^2(p_i, p_j, p_3, p_4) (2\pi)^4 \delta^{(4)}(p_i + p_j - p_3 - p_4), \end{aligned} \quad (34)$$

with the off-shell density of time-like partons  $i$  given by

$$n_i^{\text{off}}(T, \mu_q) = d_i \int \frac{d^4 p_i}{(2\pi)^4} \theta(\omega_i) 2\omega_i \tilde{\rho}_i f_i(T, \mu_q). \quad (35)$$

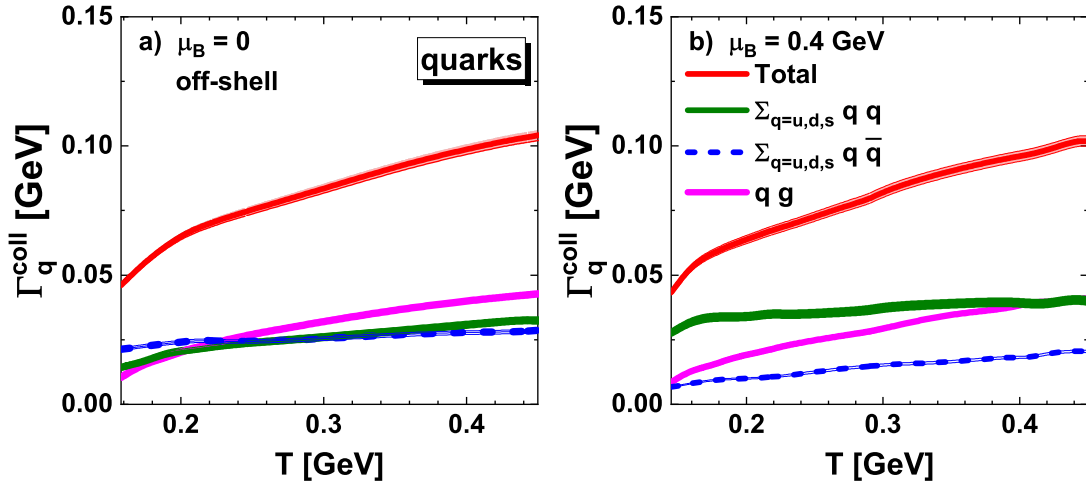


FIG. 6. (Color online) Off-shell collision rate from Eq. (34) of a light quark  $q$  as a function of the temperature  $T$  for  $\mu_B = 0$  (a) and  $\mu_B = 0.4$  GeV (b) (blue lines). The contributions from the scattering with light quarks (green), antiquarks (blue) and gluons (pink) are given by the lower hatched bands which arise from the finite statistics in the evaluation of the integrals by Monte Carlo.

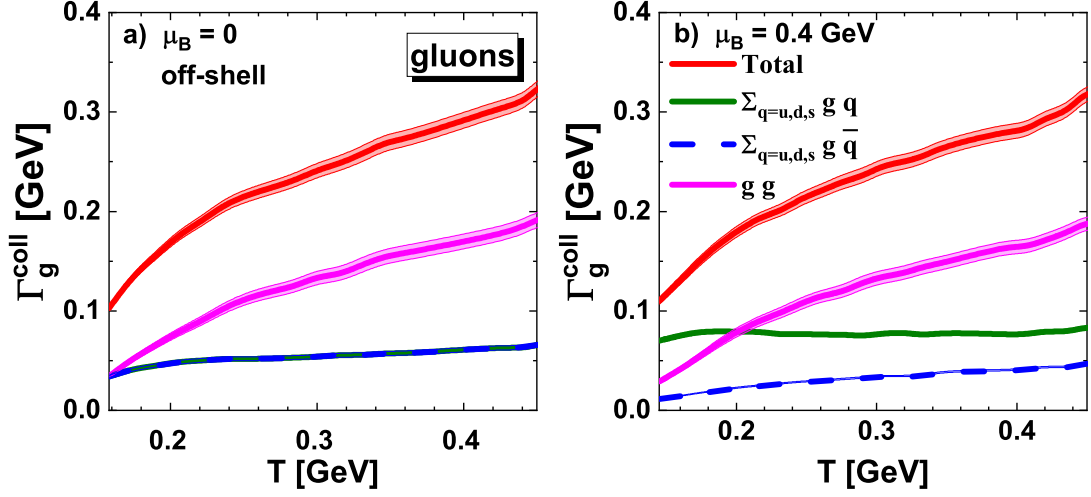


FIG. 7. (Color online) Off-shell collision rate from Eq. (34) of a gluon  $g$  as a function of the temperature  $T$  for  $\mu_B = 0$  (a) and  $\mu_B = 0.4$  GeV (b). The contributions from the scattering with light quarks (green), antiquarks (blue) and gluons (pink) are given by the lower hatched bands which arise from the finite statistics in the evaluation of the integrals by Monte Carlo.

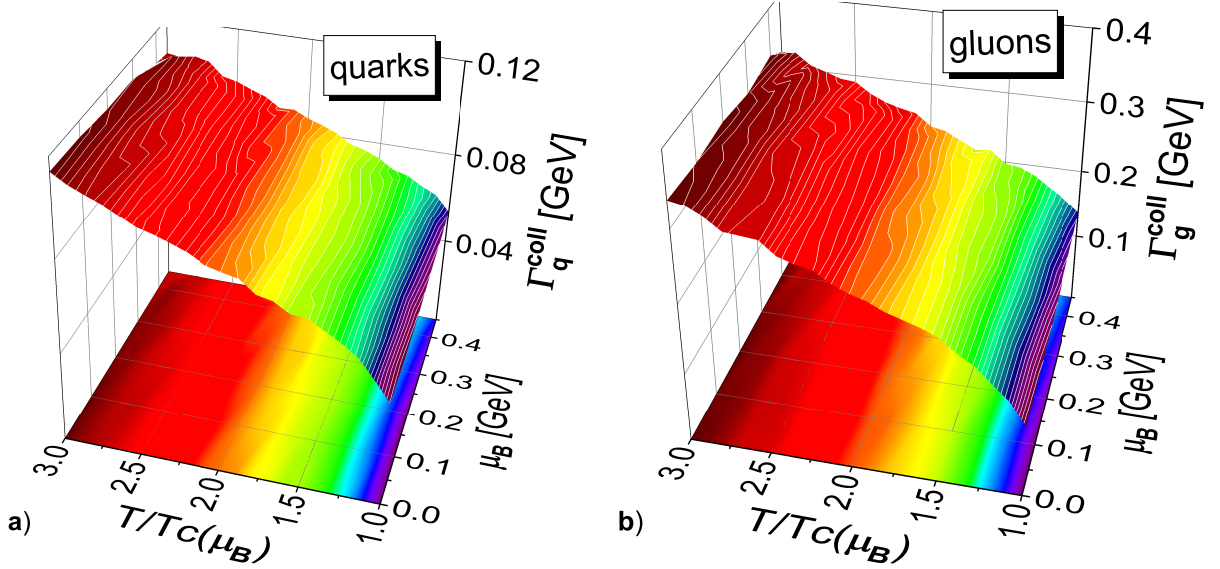


FIG. 8. (Color online) Off-shell collision rate of a quark (a) and gluon (b) as a function of the scaled temperature  $T/T_c(\mu_B)$  and the baryon chemical potential  $\mu_B$  from Eq. (34).

Fig. 6 shows the "off-shell interaction rate"  $\Gamma_q^{\text{coll}}$  of a light quark  $q$  as a function of the temperature  $T$  for  $\mu_B = 0$  (a) and  $\mu_B = 0.4$  GeV (b). The contributions from the scattering with light quarks (green), antiquarks (blue) and gluons (pink) are given by the lower hatched bands. At  $\mu_B = 0$  the total width  $\Gamma_q^{\text{coll}}$  to a large extent stems from quark-gluon scattering and increases with temperature while the contributions from scatterings with quarks and antiquarks are about equal and subdominant. At  $\mu_B = 0.4$  GeV the quarks are more abundant than the antiquarks and the contributions from scatterings with quarks increase while that from collisions

with antiquarks decrease relative to  $\mu_B = 0$ . The contributions from collisions with gluons slightly decreases also with  $\mu_B$  which can be attributed to a decrease of the cross sections with  $\mu_B$  as noted before. Fig. 7 shows the off-shell interaction rate of a gluon  $g$  as a function of the temperature  $T$  for  $\mu_B = 0$  (a) and  $\mu_B = 0.4$  GeV (b) as in case of quark scattering in Fig. 6. The contributions from the scattering with light quarks (green), antiquarks (blue) and gluons (pink) are given by the lower hatched bands. The discussion of the contributions to the total widths is very similar to the case of quark scattering and not repeated here.

In summarizing this section we find that the collisional widths for time-like partons are sizable and increase with temperature (as in the DQPM) but still remain substantially smaller than the pole masses in Fig. 2. Accordingly, a quasiparticle interpretation for time-like quanta should approximately hold.

Fig. 8, finally, gives an overview on the width  $\Gamma_q$  (a) and width  $\Gamma_g$  (b) as a function of the scaled temperature  $T/T_c(\mu_B)$  and chemical potential  $\mu_B$ . While the dependencies on temperature are similar for fixed  $\mu_B$  we see a general slight decrease of the total widths with  $\mu_B$  for fixed  $T/T_c(\mu_B)$  as discussed above.

## V. TRANSPORT PROPERTIES OF THE HOT AND DENSE QGP

The starting point to evaluate viscosity coefficients of partonic matter is the Kubo formalism [81, 82] which was used to calculate the viscosities for a previous version of the DQPM within the PHSD in a box with periodic boundary conditions (cf. Ref. [83]). We focus here on the calculation of the shear viscosity based on Refs. [84–87] which reads:

$$\eta^{\text{Kubo}}(T, \mu_q) = - \int \frac{d^4 p}{(2\pi)^4} p_x^2 p_y^2 \sum_{i=q, \bar{q}, g} d_i \frac{\partial f_i(\omega)}{\partial \omega} \rho_i(\omega, \mathbf{p})^2 \quad (36)$$

$$= \frac{1}{15T} \int \frac{d^4 p}{(2\pi)^4} \mathbf{p}^4 \sum_{i=q, \bar{q}, g} d_i ((1 \pm f_i(\omega)) f_i(\omega)) \rho_i(\omega, \mathbf{p})^2,$$

where the notation  $f_i(\omega) = f_i(\omega, T, \mu_q)$  is used for the distribution functions, and  $\rho_i$  denotes the spectral functions from Eq. (8). We note that the derivative of the distribution function accounts for the Pauli-blocking (-) and Bose-enhancement (+) factors. Following Ref. [86], we can evaluate the integral over  $\omega = p_0$  in Eq. (36) by using the residue theorem. When keeping only the leading order contribution in the width  $\gamma(T, \mu_B)$  from the residue - evaluated at the poles of the spectral function  $\omega_i = \pm \tilde{E}(\mathbf{p}) \pm i\gamma$  - we finally obtain:

$$\eta^{\text{RTA}}(T, \mu_q) = \frac{1}{15T} \int \frac{d^3 p}{(2\pi)^3} \sum_{i=q, \bar{q}, g} \quad (37)$$

$$\times \left( \frac{\mathbf{p}^4}{E_i^2 \Gamma_i(\mathbf{p}_i, T, \mu_q)} d_i ((1 \pm f_i(E_i)) f_i(E_i)) \right) + \mathcal{O}(\Gamma_i),$$

which corresponds to the expression derived in the relaxation-time approximation (RTA) [88] by identifying the interaction rate  $\Gamma$  with  $2\gamma$  as expected from transport theory in the quasiparticle limit [89]. This interaction rate  $\Gamma_i(\mathbf{p}_i, T, \mu_q)$  (inverse relaxation time) is calculated microscopically by Eq. (29). We recall that the pole energy is  $E_i^2 = p^2 + M_i^2$  where  $M_i$  is the pole mass given in the DQPM by Eqs. (4)-(5). As in the previous section,

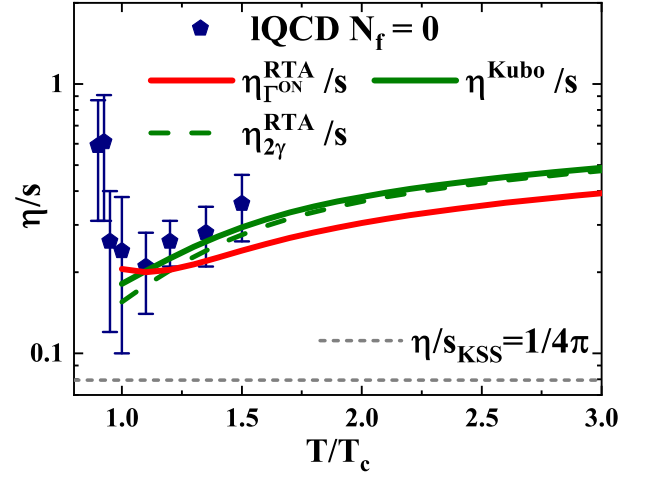


FIG. 9. (Color online) The ratio of shear viscosity to entropy density as a function of the scaled temperature  $T/T_c$  for  $\mu_B = 0$  from Eq. (36-37). The solid green line ( $\eta^{\text{Kubo}}/s$ ) shows the results from the original DQPM in the Kubo formalism while the dashed green line ( $\eta_{2\gamma}^{\text{RTA}}/s$ ) shows the same result in the quasiparticle approximation (37). The solid red line ( $\eta_{\Gamma^{\text{on}}}^{\text{RTA}}/s$ ) results from Eq. (37) using the interaction rate  $\Gamma^{\text{on}}$  (29) calculated by the microscopic differential cross sections in the on-shell limit. The dashed gray line demonstrates the Kovtun-Son-Starinets bound [90, 91] ( $\eta/s_{\text{KSS}} = 1/(4\pi)$ ), and the symbols show lQCD data for pure SU(3) gauge theory taken from Ref. [92] (pentagons).

we use here the notation  $\sum_{j=q, \bar{q}, g}$  which includes the contribution from all possible partons which in our case are the gluons and the (anti-)quarks of three different flavors ( $u, d, s$ ).

The actual results are displayed in Fig. 9 for the ratios of shear viscosity to entropy density  $\eta/s$  as a function of the scaled temperature  $T/T_c$  for  $\mu_B = 0$  in comparison to those from lattice QCD [92]. The solid green line ( $\eta^{\text{Kubo}}/s$ ) shows the result from the original DQPM in the Kubo formalism while the dashed green line ( $\eta_{2\gamma}^{\text{RTA}}/s$ ) shows the same result in the quasiparticle approximation (37) by replacing  $\Gamma_i$  by  $2\gamma_i$ . The solid red line ( $\eta_{\Gamma^{\text{on}}}^{\text{RTA}}/s$ ) results from Eq. (37) using the interaction rate  $\Gamma^{\text{on}}$  (29) calculated by the microscopic differential cross sections in the on-shell limit. We find that - apart from temperatures close to  $T_c$  - the ratios  $\eta/s$  do not differ very much and have a similar behavior as a function of temperature. The approximation (37) of the shear viscosity is found to be very close to the one from the Kubo formalism (36) indicating that the quasiparticle limit ( $\gamma \ll M$ ) holds in the DQPM. We have also checked that the shear viscosity does not differ substantially if one uses the momentum-dependent interaction rate from Eq. (29) or the averaged one from Eq. (31).

An overview for the ratio of shear viscosity to entropy density  $\eta/s$  as a function of the scaled temperature  $T/T_c(\mu_B)$  and  $\mu_B$  is given Fig. 10 in case of the Kubo formalism (a) (36) and the on-shell limit (37) (b). There



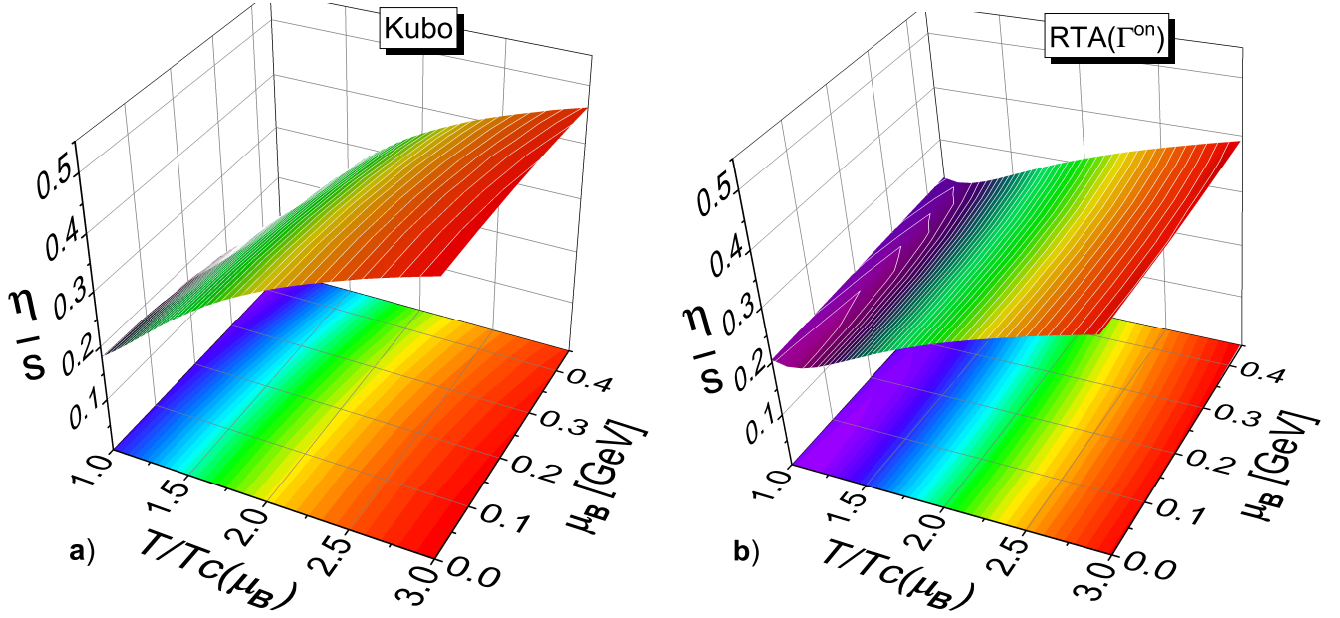


FIG. 10. (Color online) The ratio of shear viscosity to entropy density  $\eta/s$  as a function of the scaled temperature  $T/T_c(\mu_B)$  and baryon chemical potential  $\mu_B$  calculated within the Kubo formalism (a) from Eq. (36) and in the Relaxation Time Approximation (RTA) (b) from Eq. (37) using the on-shell interaction rate  $\Gamma^{\text{on}}$  from Eq. (29).

is no strong variation with  $\mu_B$  for fixed  $T/T_c(\mu_B)$ , however, the ratio increases slightly with  $\mu_B$  in the on-shell limit while it slightly drops with  $\mu_B$  in the Kubo formalism for the DQPM. Accordingly, there is some model uncertainty when extracting the shear viscosity in the different approximations.

In summarizing this section we find that the results for the ratio of shear viscosity over entropy density from the original DQPM and those from the microscopic calculations are similar and within error bars compatible with present results from lattice QCD. However, having the differential cross sections for each partonic channel at hand one might find substantial differences for non-equilibrium configurations as encountered in relativistic heavy-ion collisions where a QGP is formed initially out-of-equilibrium.

## VI. EXTRACTION OF $T$ AND $\mu_B$ FROM PHSD IN HEAVY-ION COLLISIONS

Since PHSD is a microscopic off-shell transport approach it does not incorporate thermodynamic Lagrange parameters such as  $T$  and  $\mu_B$  that characterize the system in equilibrium. In order to extract the required information (the temperature  $T$  and baryon chemical potential  $\mu_B$ ) - defining the parton properties and differential scattering processes in the PHSD space-time grid - we construct the DQPM equation of state ( $P^{\text{EoS}}, n_B^{\text{EoS}}, s^{\text{EoS}}, \epsilon^{\text{EoS}}$ ) starting from the expansion of thermodynamic quantities in terms of the 2<sup>nd</sup> order baryon number susceptibility  $\chi_2^B = \partial^2 P / \partial \mu_B^2|_{\mu_B=0}$  as:

$$\Delta P/T^4 = \frac{P(T, \mu_B) - P(T, 0)}{T^4} \approx \frac{1}{2} \chi_2^B(T) \left( \frac{\mu_B}{T} \right)^2, \quad (38)$$

$$\frac{n_B}{T^3} = \left. \frac{\partial(P/T^4)}{\partial(\mu_B/T)} \right|_T \approx \chi_2^B(T) \left( \frac{\mu_B}{T} \right), \quad (39)$$

$$\begin{aligned} \Delta s/T^3 &= \frac{s(T, \mu_B) - s(T, 0)}{T^3} = \frac{1}{T^3} \left. \frac{\partial \Delta P}{\partial T} \right|_{\mu_B} \\ &= T \left. \frac{\partial(\Delta P/T^4)}{\partial T} \right|_{\mu_B} + 4(\Delta P/T^4) \\ &\approx \frac{1}{2} \left( T \frac{\partial \chi_2^B(T)}{\partial T} + 2\chi_2^B(T) \right) \left( \frac{\mu_B}{T} \right)^2, \end{aligned} \quad (40)$$

$$\begin{aligned} \Delta \epsilon/T^4 &= \frac{\epsilon(T, \mu_B) - \epsilon(T, 0)}{T^4} \\ &= \Delta s/T^3 - \Delta P/T^4 + \left( \frac{\mu_B}{T} \right) \frac{n_B}{T^3} \\ &\approx \frac{1}{2} \left( T \frac{\partial \chi_2^B(T)}{\partial T} + 3\chi_2^B(T) \right) \left( \frac{\mu_B}{T} \right)^2. \end{aligned} \quad (41)$$

From the DQPM pressure at  $\mu_B = 0$  and the 2<sup>nd</sup> order baryon number susceptibility  $\chi_2^B$ , one can deduce all thermodynamics according to the previous formulae. For the DQPM pressure at  $\mu_B = 0$  we employ the parametrization of lQCD data provided in Ref. [71] considering the very good agreement between lQCD data

and the DQPM in Fig. 3. In addition, a parametrization of the DQPM 2<sup>nd</sup> order baryon number susceptibility from Refs. [63, 64] is used. Note that this parametrization of  $\chi_2^B$  is also in agreement with lQCD data below  $T_c$  which allows for an evaluation of  $T$  and  $\mu_B$  also in the hot hadronic phase. We point out that these results have to be taken as estimates in the regions of large chemical potentials and below the critical temperature  $T_c$ . Furthermore, the DQPM 2<sup>nd</sup> order baryon number susceptibility 2<sup>nd</sup> is found to be slightly lower compared to lQCD results (see Ref. [63, 64]) which therefore leads to a slight overestimation of the baryon chemical potential  $\mu_B$ .

In each space-time cell of the PHSD grid, the thermodynamic quantities are calculated by the method developed in Ref. [93], i.e. by diagonalization of the energy momentum tensor  $T^{\mu\nu}$  as:

$$T^{\mu\nu} (x_\nu)_i = \lambda_i (x^\mu)_i = \lambda_i g^{\mu\nu} (x_\nu)_i, \quad (42)$$

with  $i = 0, 1, 2, 3$ , where  $\lambda_i$  are the eigenvalues of  $T^{\mu\nu}$  and  $(x_\nu)_i$  are the corresponding eigenvectors. For  $i = 0$ , the local energy density  $\epsilon$  is identified with the eigenvalue of  $T^{\mu\nu}$  (Landau matching) and the corresponding time-like eigenvector is defined as the 4-velocity  $u_\nu$ :

$$T^{\mu\nu} u_\nu = \epsilon u^\mu = (\epsilon g^{\mu\nu}) u_\nu \quad (43)$$

using the normalization condition  $u^\mu u_\mu = 1$ . The three other solutions are  $(-P_i)$ , the pressure components expressed in the local rest frame of the cell. The energy-momentum tensor  $T^{\mu\nu}$  is calculated in PHSD as:

$$T^{\mu\nu} = \sum_i \frac{p_i^\mu p_i^\nu}{E_i}, \quad (44)$$

where the sum  $i$  runs over all the particles in the considered cell.

In the beginning of heavy-ion collisions the created medium is highly anisotropic due to the longitudinal expansion. In order to correct for the anisotropy we apply the *shape generalized equation of state* developed in Ref. [94] in order to extract values for the temperature  $T$  and baryon chemical potential  $\mu_B$ . In this framework, the energy density  $\epsilon^{\text{anis}}$  and pressure components of an anisotropic medium are evaluated by the following expressions:

$$\epsilon^{\text{anis}} = \epsilon^{\text{EoS}} r(x) \quad (45)$$

$$P_\perp = P^{\text{EoS}} [r(x) + 3xr'(x)] \quad (46)$$

$$P_\parallel = P^{\text{EoS}} [r(x) - 6xr'(x)], \quad (47)$$

where  $P_\perp$  and  $P_\parallel$  are, respectively, the transverse and

longitudinal pressures, and  $\epsilon^{\text{EoS}}$  and  $P^{\text{EoS}}$  are the equilibrium energy density and pressure from which a temperature  $T$  and chemical potential  $\mu_B$  can be extracted. The anisotropy parameter  $x$  can be approximated as a function of the pressure components as  $P_\parallel/P_\perp = x^{-3/4}$ , and the function  $r(x)$  reads:

$$r(x) = \begin{cases} \frac{x^{-1/3}}{2} \left[ 1 + \frac{x \operatorname{arctanh} \sqrt{1-x}}{\sqrt{1-x}} \right] & \text{for } x \leq 1 \\ \frac{x^{-1/3}}{2} \left[ 1 + \frac{x \operatorname{arctan} \sqrt{x-1}}{\sqrt{x-1}} \right] & \text{for } x \geq 1. \end{cases} \quad (48)$$

In a PHSD simulation, we calculate in each of the cells the energy density  $\epsilon^{\text{PHSD}}$ , the baryon density  $n_B^{\text{PHSD}}$ , as well as the pressure components  $P_\perp^{\text{PHSD}}$  and  $P_\parallel^{\text{PHSD}}$ , from which one can evaluate the function  $r(x)$  in Eq. (48). In order to find the temperature  $T$  and baryon chemical potential  $\mu_B$  according to the DQPM EoS - constructed at the beginning of this section VI - we have to solve the following system of equations:

$$\begin{cases} \epsilon^{\text{EoS}}(T, \mu_B) = \epsilon^{\text{PHSD}}/r(x) \\ n_B^{\text{EoS}}(T, \mu_B) = n_B^{\text{PHSD}} \end{cases} \quad (49)$$

where the left-hand sides represent the DQPM EoS which depends on the unknowns  $T$  and  $\mu_B$ , whereas on the right-hand sides of these equations we have the energy density and baryon density evaluated in PHSD. In Eq. (49) the energy density from PHSD  $\epsilon^{\text{PHSD}}$  is divided by the function  $r(x)$  from Eq. (48) to account for the anisotropy of the considered cell according to the *shape generalized equation of state* in Eq. (45). We solve this system by using the Newton-Raphson method [95, 96]. Since for a given energy density and baryon density one can obtain two different solutions for  $T$  and  $\mu_B$  in Eq. (49), the isotropic pressure  $P^{\text{EoS}}$  calculated from  $P_\perp^{\text{PHSD}}$ ,  $P_\parallel^{\text{PHSD}}$ , the function  $r(x)$  and its derivative  $r'(x)$  in Eqs. (46)-(47), is also used to initialize the algorithm in order to find the correct solution. We show in Fig. 11 the results from our algorithm in the  $T - \mu_B$  plane using as input varying values of energy density for fixed baryon densities  $n_B$ . The black line corresponds to the DQPM critical temperature and the dashed grey lines correspond to different values of  $\mu_B/T$  for orientation. In Fig. 12 isentropic trajectories are shown corresponding to a fixed number of the entropy density over the baryon density  $s/n_B$ . According to Ref. [97], these different values of  $s/n_B$  correspond to the trajectories of heavy-ion collisions from the beam energy scan program at RHIC ( $\sqrt{s_{NN}} = 200$  GeV, 62.4 GeV, 39 GeV, 27 GeV, 19.6 GeV and 14.5 GeV).

We now turn to the evaluation of  $T$  and  $\mu_B$  in actual PHSD simulations for Au+Au collisions. In the evaluation of the energy density and the baryon density  $n_B$  leading baryons or diquarks are discarded since these are

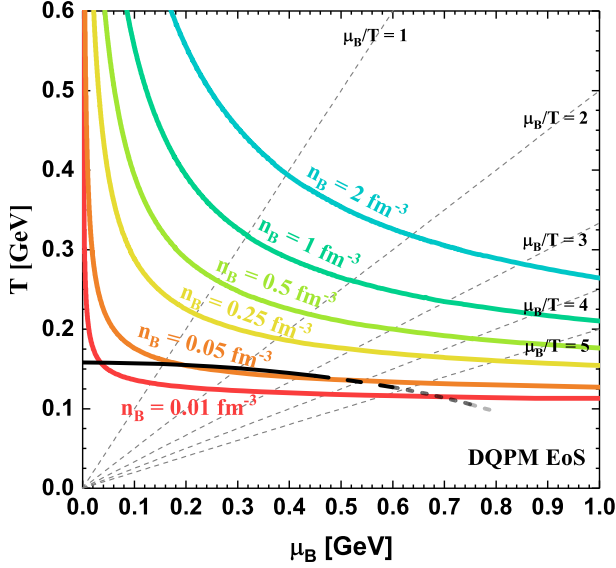


FIG. 11. (Color online) Extraction of  $T$  and  $\mu_B$  according to the equation of state constructed from DQPM. The different lines correspond to a fixed value of baryon density  $n_B$ . The black line corresponds to the DQPM critical temperature and the dashed grey lines correspond to different values of  $\mu_B/T$  for orientation.

almost located at target or projectile rapidity. As an example for our results we show in Fig. 13 the ratio  $\mu_B/T$  as a function of the cell rapidity  $y_{\text{cell}}$  at different times (from 0.5 to 6 fm/c) for 5% central Pb+Pb collisions at 158 A GeV. The largest ratios are seen for all times for rapidities closer to projectile and target rapidities (cf. Ref. [53]) while at midrapidity this ratio is initially high (at  $t = 0.5$  fm/c), but drops practically to zero at  $t = 2$  fm/c and increases later on up to values of order 1. We mention that this profile is very close to that calculated in the hydrodynamics + hadronic transport approach by Denicol et al. (Fig. 5 in Ref. [51]) and also shows an increase of  $\mu_B/T$  with increasing  $|y|$ .

Fig. 14 shows the temperature profile (for the central cell) as a function of the cell rapidity  $y_{\text{cell}}$  and different times (from 0.15 to 7 fm/c) for a 5% central Au+Au collision at  $\sqrt{s_{NN}} = 200$  GeV. This temperature profile initially ( $t = 0.15$  fm/c) has a broad maximum at midrapidity but for  $t > 0.25$  fm/c slight maxima at  $|y_{\text{cell}}| \approx 1.5$  appear which move to higher cell rapidity with increasing time while the average temperature drops rapidly in time. The lowest temperatures (at midrapidity), however, are still on the level of 250 MeV at  $t = 2$  fm/c, i.e. well above the critical temperature  $T_c$ . We note in passing that the temperature profiles from two different extraction methods, directly from the energy density of the cell in PHSD  $\epsilon^{\text{PHSD}}$  (dashed lines) - setting  $r(x) = 1$  in Eq. (49) - and from the equation of state  $\epsilon^{\text{EoS}}$  (solid lines) are practically the same for  $t \geq 0.25$  fm/c and provide an idea about the accuracy of our extraction method.

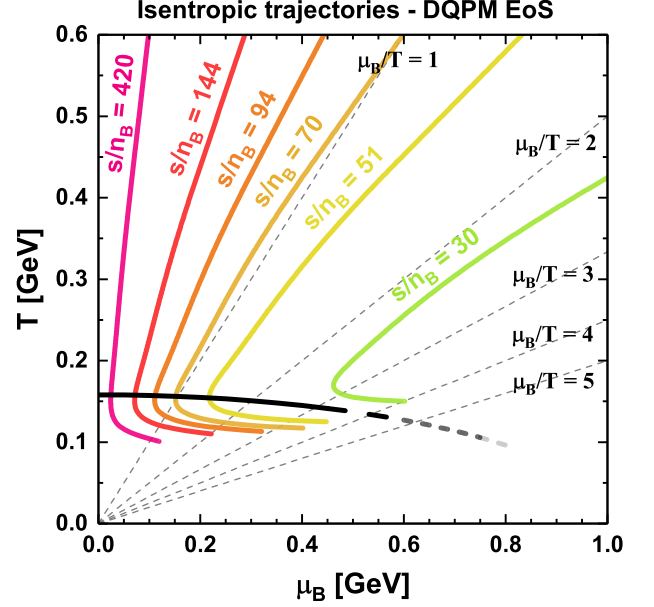


FIG. 12. (Color online) Isentropic trajectories for different ratios of the entropy density over the baryon density  $s/n_B$ . The black line corresponds to the DQPM critical temperature and the dashed grey lines correspond to different value of  $\mu_B/T$  for orientation.

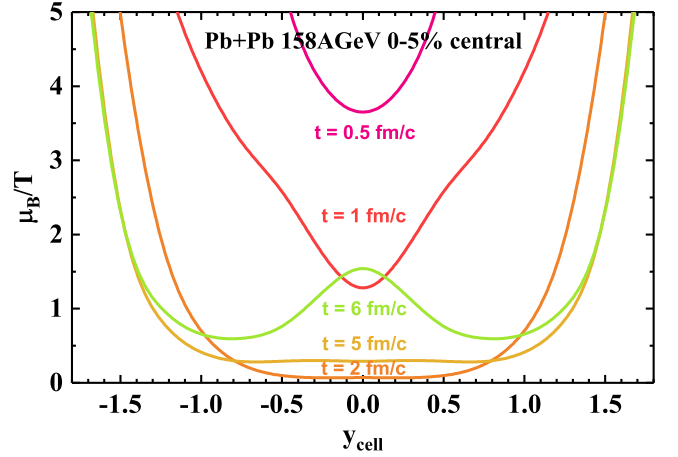


FIG. 13. (Color online) The ratio  $\mu_B/T$  as a function of the cell rapidity  $y_{\text{cell}}$  at different times  $t$  for 5% central Pb+Pb collisions at 158 A GeV from PHSD.

We now focus on the time evolution of the distribution in  $T$  and  $\mu_B$  for cells having a temperature  $T > T_c(\mu_B)$  at midrapidity ( $|y_{\text{cell}}| < 0.5$ ) for 5% central heavy-ion collisions. Fig. 15 (a) shows this distribution for a Au+Au collision at  $\sqrt{s_{NN}} = 200$  GeV from PHSD for times  $t < 0.5$  fm/c,  $0.5$  fm/c  $< t < 2$  fm/c and  $t > 2$  fm/c. The scale corresponds to the number of cells in the PHSD event in the considered bin in  $T - \mu_B$  divided by the total number of cells in the corresponding time window while the solid black line is the DQPM phase boundary

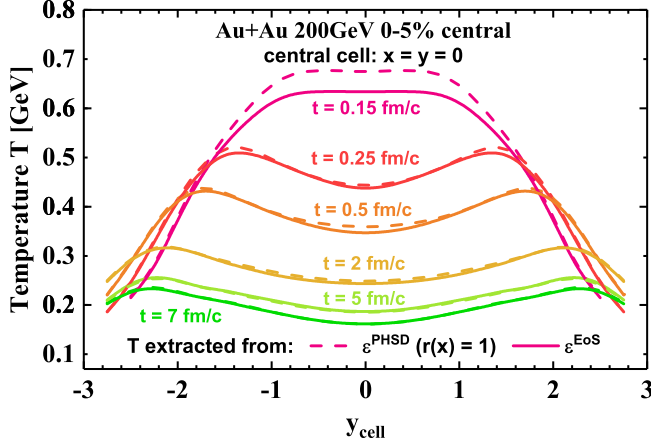


FIG. 14. (Color online) The temperature profile (for the central cell) as a function of the cell rapidity  $y_{\text{cell}}$  and different times (from 0.15 to 7 fm/c) for a 5% central Au+Au collision at  $\sqrt{s_{NN}} = 200$  GeV from PHSD. The dashed lines result when extracting the temperature directly from the energy density of the central cell in PHSD  $\epsilon^{\text{PHSD}}$  while the solid lines refer to the extraction from the equation of state  $\epsilon^{\text{EoS}}$  (see text).

for orientation. At the very early times  $t < 0.5$  fm/c the distribution peaks at  $T \approx 0.35$  GeV and is shifted to small positive average  $\mu_B$ , however, is rather broad in  $T$  and  $\mu_B$ . For times  $0.5 \text{ fm/c} < t < 2 \text{ fm/c}$  the average temperature has dropped to about 0.24 GeV and is localized at small average  $\mu_B$  while the widths of the distribution remain sizable. For later times ( $t > 2 \text{ fm/c}$ ) the distribution peaks at an average temperature slightly above  $T_c$  but stays broad in  $\mu_B$ . Note that a negative  $\mu_B$  implies that there are more antiquarks (antibaryons) than quarks (baryons) in the individual cell. This time evolution of the distribution at the top RHIC energy matches well known expectations, however, the actual widths in  $\mu_B$  turn out to be quite large.

Fig. 15 (b) shows the distribution in  $T$  and  $\mu_B$  for cells at midrapidity ( $|y_{\text{cell}}| < 0.5$ ) in case of Pb+Pb collisions at 158 A GeV from PHSD for times  $t < 1 \text{ fm/c}$ ,  $1 \text{ fm/c} < t < 2 \text{ fm/c}$  and  $t > 2 \text{ fm/c}$ . For early times  $t < 1 \text{ fm/c}$  the distribution peaks at a temperature of about 0.28 GeV and a sizable chemical potential of about 0.35 GeV while for times in the interval  $1 \text{ fm/c} < t < 2 \text{ fm/c}$  the maximum has dropped already to an average temperature  $\sim 0.18$  GeV and small chemical potential. This is due to the fact that baryons practically no longer appear in the central cell and quarks and antiquarks are almost equal in number. For later times  $t > 2 \text{ fm/c}$  the distribution (above  $T_c$ ) essentially has broadened widely in  $\mu_B$  without characteristic peak at a possible critical point.

We close this section by visualizing in Fig. 16 the space-time distribution of the extracted temperatures (left column) and chemical potentials  $\mu_B$  (right column) for a 5% central collision of Pb+Pb at 158 A GeV from PHSD. These distributions correspond to the transverse

plane  $(x, y)$  - orthogonal to the beam direction - at  $z = 0$ , i.e. in the center of the collision zone. For early times we find the temperatures of the fireball to be well above  $T_c$  practically everywhere with a maximum in the center. Then the fireball expands in space with time while the temperature drops accordingly. At  $t = 6 \text{ fm/c}$  the temperature is above  $T_c$  only in the central region and the spiky distribution in the surface region indicates blobs of hadronized matter. This is in line with the common picture of fireball expansion and hadronization. However, the profile in the chemical potential  $\mu_B$  (right column) shows that the  $\mu_B$  is sizable only for very early times in the whole fireball and drops to almost zero in the hot QGP zone for  $t = 2 \text{ fm/c}$  while staying finite at the surface of the fireball. The subsequent hadronization in the surface is visualized again by the finite  $\mu_B$  drops at  $t = 6 \text{ fm/c}$ . The local QGP region thus is of low baryon chemical potential, which has not been expected so far at this bombarding energy.

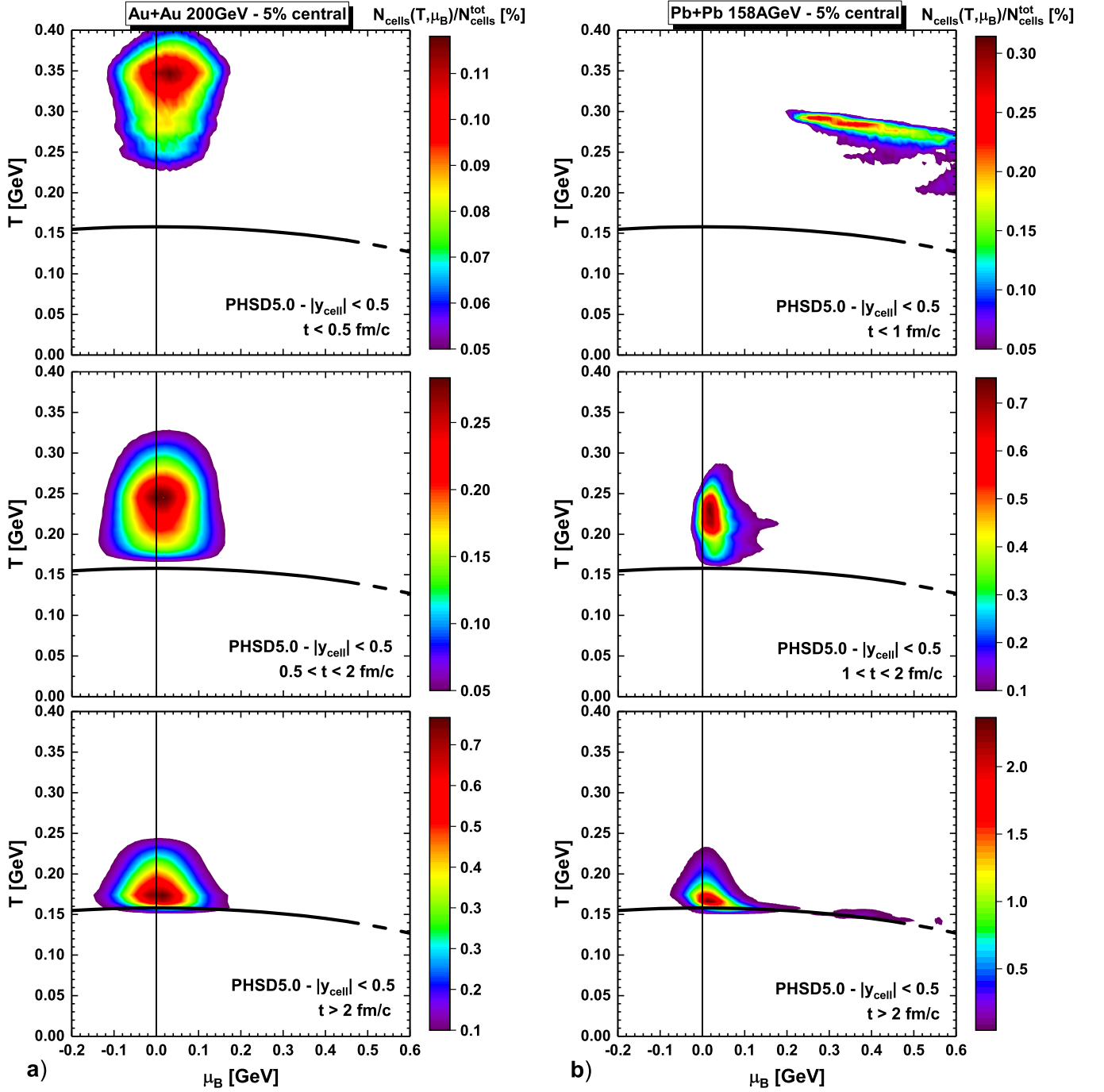


FIG. 15. (Color online) Distributions in  $T$  and  $\mu_B$  as extracted from the DQPM equation of state in a PHSD simulation of a central Au+Au collision at  $\sqrt{s_{NN}} = 200$  GeV (a) and of a central Pb+Pb collision at 158 A GeV (b) for cells with a temperature  $T > T_c(\mu_B)$ . The scale corresponds to the number of cells in the PHSD event in the considered bin in  $T - \mu_B$  divided by the total number of cells in the corresponding time window (see legend). The solid black line is the DQPM phase boundary for orientation while the vertical line stands for  $\mu_B = 0$ .



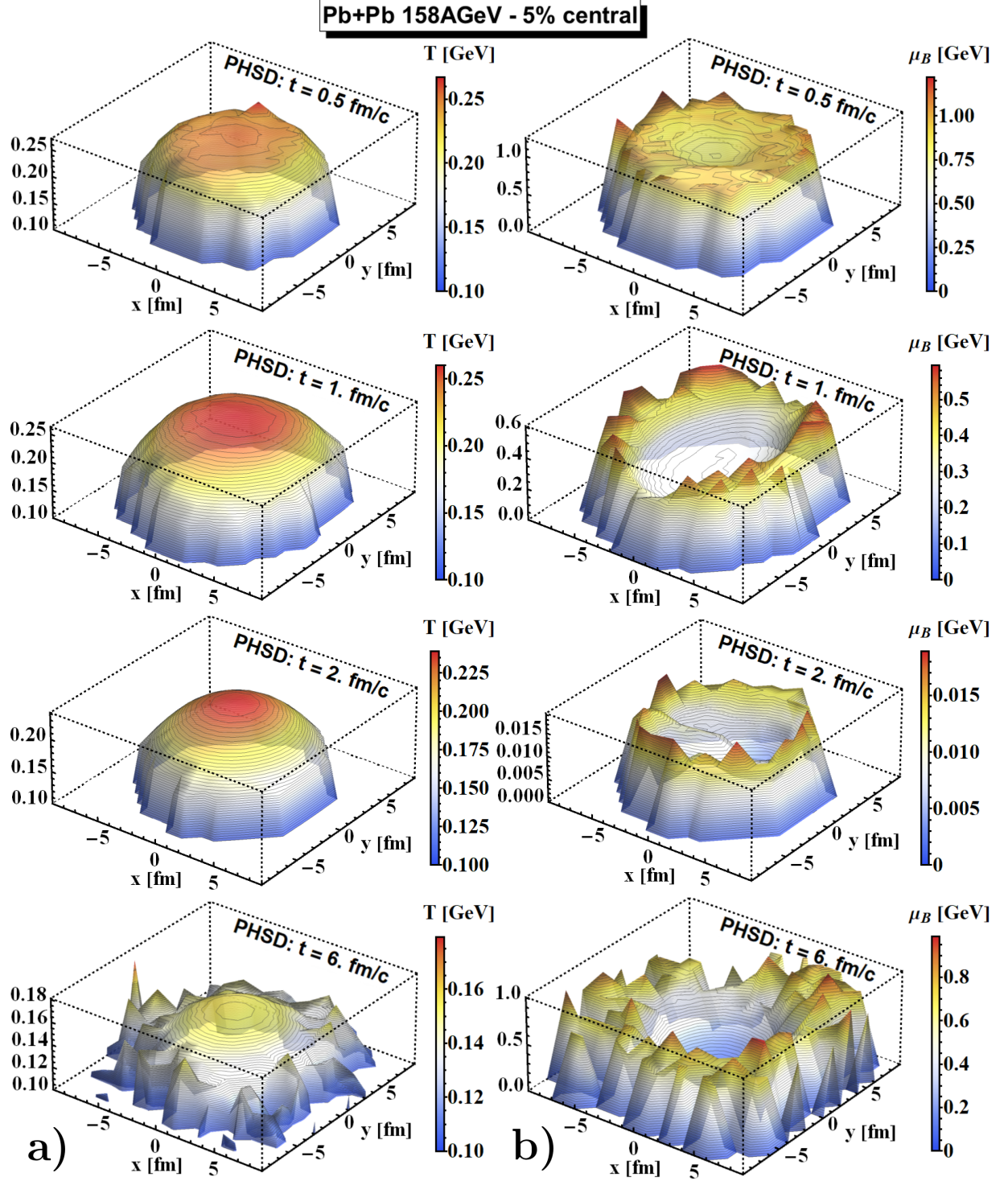


FIG. 16. (Color online) (left) The temperature profile in  $(x, y)$  (at  $z = 0$ ) for different times from 0.5 to 6 fm/c in case of a 5% central Pb+Pb collision at 158 A GeV from PHSD. (right) The profile in the chemical potential  $\mu_B$  in  $(x, y)$  (at  $z = 0$ ) for different times from 0.5 to 6 fm/c for the same collision.

## VII. OBSERVABLES FROM RELATIVISTIC NUCLEUS-NUCLEUS COLLISIONS

As mentioned above the PHSD transport approach [54, 58] is a microscopic covariant dynamical model for strongly interacting systems formulated on the basis of Kadanoff-Baym equations [26] for Green's functions in phase-space representation (in first order gradient expansion beyond the quasiparticle approximation). The approach consistently describes the full evolution of a relativistic heavy-ion collision from the initial hard scatterings and string formation through the dynamical deconfinement phase transition to the strongly-interacting quark-gluon plasma (sQGP) as well as hadronization and the subsequent interactions in the expanding hadronic phase as in the Hadron-String-Dynamics (HSD) transport approach [98]. Note that at lower bombarding energies - without any partonic phase - the PHSD approach merges to the HSD approach with only hadronic and string degrees of freedom. Since we only look for modifications in the partonic phase - cf. Sections III and IV, we do not further specify the hadronic sector and refer the reader to Refs. [45, 46, 98] for details. We recall that in the PHSD4.0 version, the partonic cross sections are parametrized as a function of the energy density to comply with the individual widths of quarks, antiquarks and gluons (cf. Ref. [56]), while the parton masses are parametrized as a function of the scalar density (cf. Ref. [58]).

### A. AGS-SPS energies

We start with lower and intermediated energies covered experimentally by the AGS (BNL) and SPS (CERN) with a focus on central Au+Au or Pb+Pb collisions. We will compare results for the "bulk" observables (rapidity distributions and  $p_T$ - or  $m_T$ -spectra) from PHSD calculations based on the default DQPM parameters (PHSD4.0) with the new PHSD5.0 including the differential cross sections from section III for the individual partonic channels at finite  $T$  and  $\mu_B$  as well as the parton masses  $M_i(T, \mu_B)$  from Eqs. (4)-(5). A comparison to the available experimental data is included (for orientation) but not discussed explicitly since this has been done in earlier work in detail [45, 46, 55].

Fig. 17 displays the actual results for hadronic rapidity distributions in case of 5% central Au+Au collisions at 10.7 A GeV for PHSD4.0 (green dot-dashed lines), PHSD5.0 with partonic cross sections and parton masses calculated for  $\mu_B = 0$  (blue dashed lines), and with cross sections and parton masses evaluated at the actual chemical potential  $\mu_B$  in each individual space-time cell (red lines) in comparison to the experimental data from the E866 [99], E877 [100], E891 [101], E877 [102] and E896 [103] collaborations. Here we focus on the most abundant hadrons, i.e. pions, kaons, protons and neutral hyperons. We note in passing that the effects of chiral symmetry

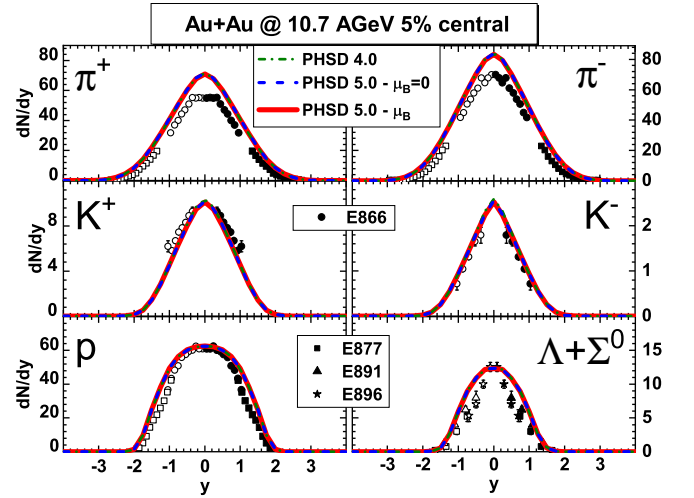


FIG. 17. (Color online) The rapidity distributions for 5% central Au+Au collisions at 10.7 A GeV for PHSD4.0 (green dot-dashed lines), PHSD5.0 with partonic cross sections and parton masses calculated for  $\mu_B = 0$  (blue dashed lines) and with cross sections and parton masses evaluated at the actual chemical potential  $\mu_B$  in each individual space-time cell (red lines) in comparison to the experimental data from the E866 [99], E877 [100], E891 [101], E877 [102] and E896 [103] collaborations. All PHSD results are the same within the linewidth.

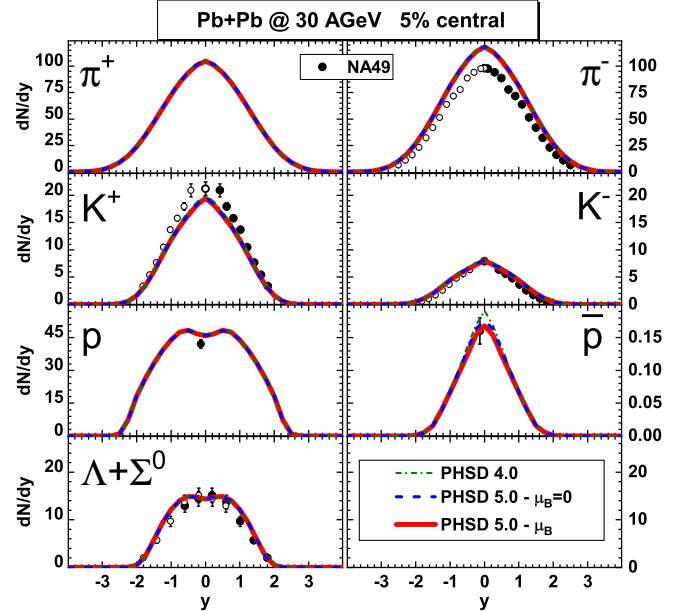


FIG. 18. (Color online) The rapidity distributions for 5% central Pb+Pb collisions at 30 A GeV for PHSD4.0 (green dot-dashed lines), PHSD5.0 with partonic cross sections and parton masses calculated for  $\mu_B = 0$  (blue dashed lines) and with cross sections and parton masses evaluated at the actual chemical potential  $\mu_B$  in each individual space-time cell (red lines) in comparison to the experimental data from the NA49 Collaboration [104–106]. All PHSD results are practically the same within the linewidth.

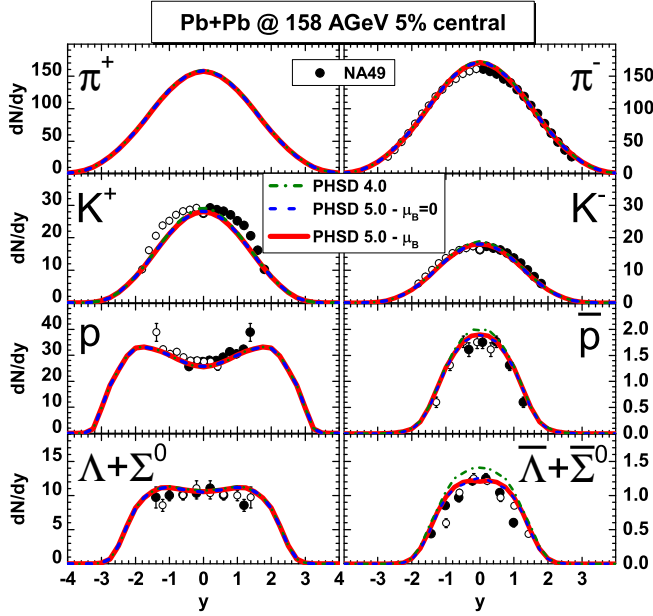


FIG. 19. (Color online) The rapidity distributions for 5% central Pb+Pb collisions at 158 A GeV for PHSD4.0 (green dot-dashed lines), PHSD5.0 with partonic cross sections and parton masses calculated for  $\mu_B = 0$  (blue dashed lines) and with cross sections and parton masses evaluated at the actual chemical potential  $\mu_B$  in each individual space-time cell (red lines) in comparison to the experimental data from the NA49 Collaboration [107–110]. All PHSD results are the same within the linewidth except for the antibaryons.

restoration are incorporated as in Refs. [45, 46] since this was found to be mandatory to achieve a reasonable description of the strangeness degrees of freedom reflected in the kaon and neutral hyperon dynamics. As seen from Fig. 17 there is no difference in rapidity distributions for all the hadron species from the different versions of PHSD within linewidth which implies that there is no sensitivity to the new partonic differential cross sections and parton masses employed. One could argue that this result might be due to the low amount of QGP produced at this energy but the different PHSD calculations for 5% central Pb+Pb collisions at 30 A GeV in Fig. 18 for the hadronic rapidity distributions do not provide a different picture, too. Only when stepping up to the top SPS energy of 158 A GeV one can identify a small difference in the antibaryon sector ( $\bar{p}$ ,  $\bar{\Lambda}$  +  $\bar{\Sigma}^0$ ) in case of 5% central Pb+Pb collisions (cf. Fig. 19).

According to the studies above there is apparently no sizable sensitivity in the hadronic rapidity distributions to the actual differential partonic cross sections, but one has to explore the transverse dynamics in addition. To this end we show in Figs. 21 and 22 the transverse momentum distributions for 5% central Pb+Pb collisions at 158 A GeV and midrapidity ( $|y| < 0.5$ ) for PHSD4.0 (green lines), PHSD5.0 with partonic cross sections and parton masses calculated for  $\mu_B = 0$  (blue lines) and with cross sections and parton masses evaluated at the actual

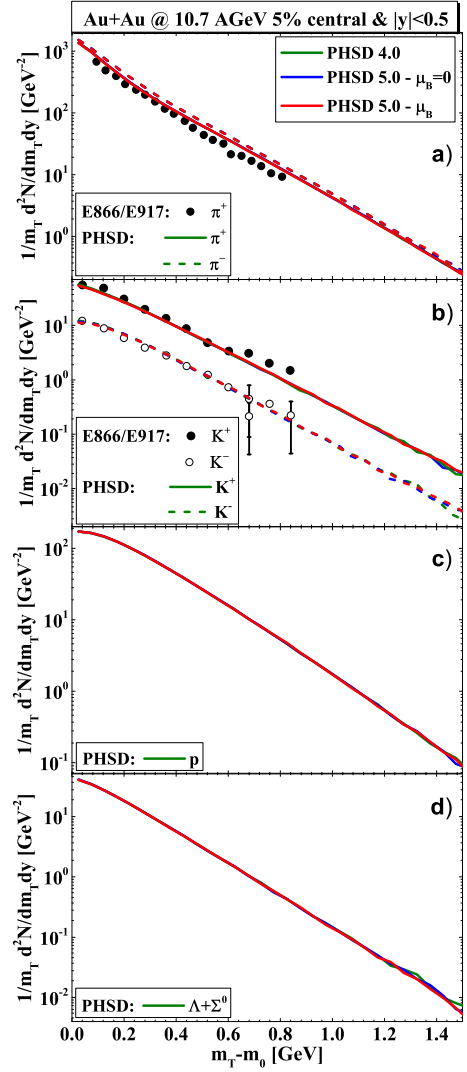


FIG. 20. (Color online) The transverse momentum distributions for 5% central Pb+Pb collisions at 11 A GeV and midrapidity ( $|y| < 0.5$ ) for PHSD4.0 (green lines), PHSD5.0 with partonic cross sections and parton masses calculated for  $\mu_B = 0$  (blue lines) and with cross sections and parton masses evaluated at the actual chemical potential  $\mu_B$  in each individual space-time cell (red lines) in comparison to the experimental data from the E917 and E866 collaborations [111, 112].

chemical potential  $\mu_B$  in each individual space-time cell (red lines) in comparison to the experimental data from the NA49 Collaboration [104–109]. Here the solid lines stand for positively charged particles while the dashed lines display the results for negatively charged particles. We find that at 30 A GeV there is practically no change in the  $p_T$  spectra for all PHSD versions; only at 158 A GeV tiny changes in the  $p_T$  spectra become visible for transverse momenta above about 2.5 GeV/c. We mention for completeness that again for 10.7 A GeV Au+Au collisions we do not find any changes also in the  $p_T$  spectra within the linewidth (cf. Fig. 20). Apparently, the space-time volume of the partonic phase is too small at

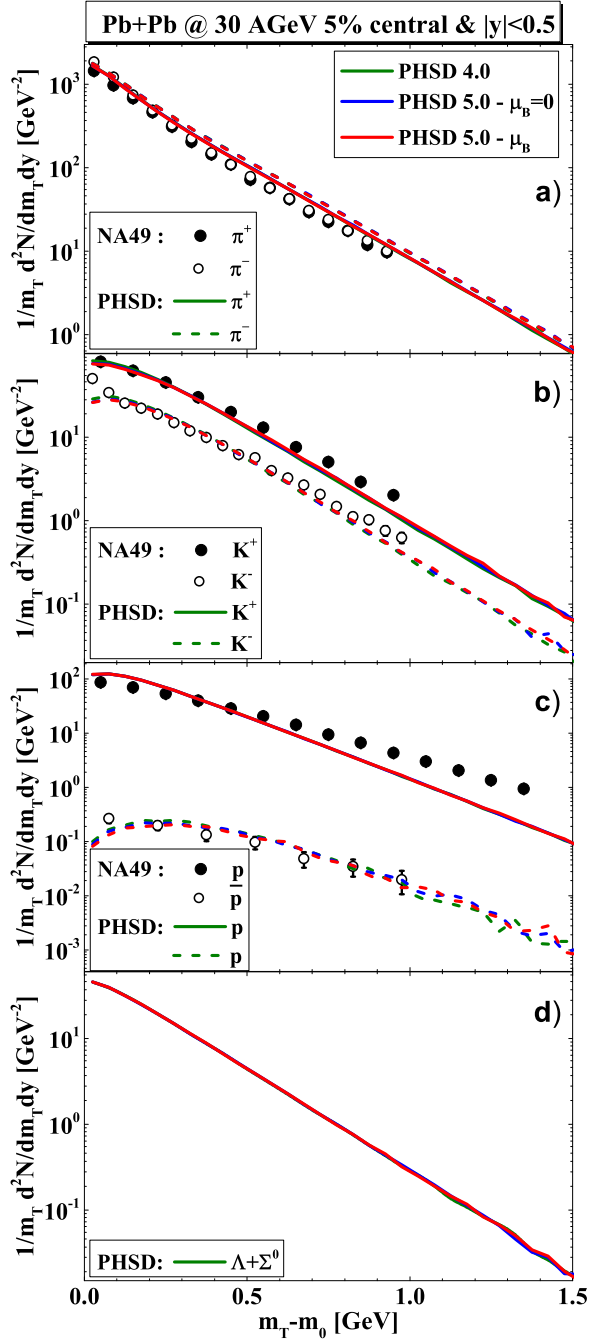


FIG. 21. (Color online) The transverse momentum distributions for 5% central Pb+Pb collisions at 30 A GeV and midrapidity ( $|y| < 0.5$ ) for PHSD4.0 (green lines), PHSD5.0 with partonic cross sections and parton masses calculated for  $\mu_B = 0$  (blue lines) and with cross sections and parton masses evaluated at the actual chemical potential  $\mu_B$  in each individual space-time cell (red lines) in comparison to the experimental data from the NA49 Collaboration [104–106].

AGS and SPS energies even in central Pb+Pb collisions such that one has practically no sensitivity to the microscopic collisional details in the partonic phase. However, this might change for ultra-relativistic collision systems

where the QGP phase becomes dominant.

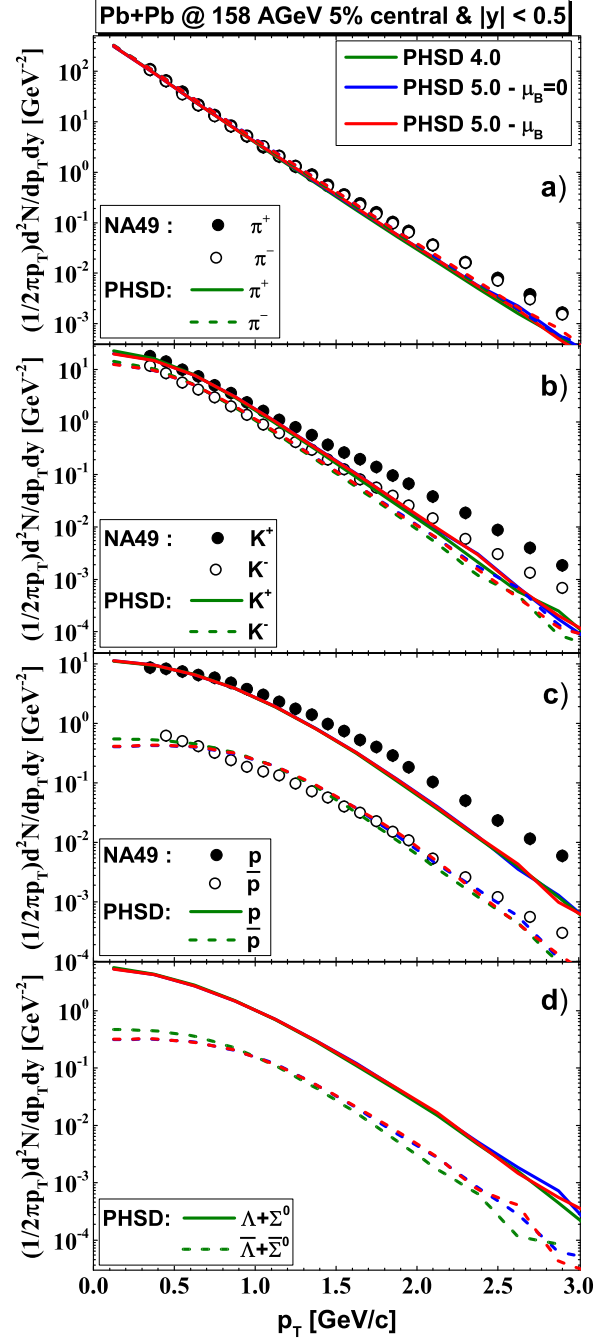


FIG. 22. (Color online) The transverse momentum distributions for 5% central Pb+Pb collisions at 158 A GeV and midrapidity ( $|y| < 0.5$ ) for PHSD4.0 (green lines), PHSD5.0 with partonic cross sections and parton masses calculated for  $\mu_B = 0$  (blue lines) and with cross sections and parton masses evaluated at the actual chemical potential  $\mu_B$  in each individual space-time cell (red lines) in comparison to the experimental data from the NA49 Collaboration [107–109].



## B. RHIC energies

As demonstrated in Ref. [58] one expects a dominantly partonic phase in central Au+Au collisions at  $\sqrt{s_{NN}} = 200$  GeV especially when gating on midrapidity. However, the differences between PHSD4.0 and PHSD5.0 (with and without  $\mu_B$ -dependence) in the hadronic rapidity distributions for 5% central Au+Au collisions turn out to be rather small for mesons ( $\pi^\pm$ ,  $K^\pm$ ) and also for baryons and antibaryons ( $p$ ,  $\bar{p}$ ,  $\Lambda + \Sigma^0$ ,  $\bar{\Lambda} + \bar{\Sigma}^0$ ) (cf. Fig. 23) such that no robust conclusion on the partonic collisional dynamics can be drawn even in this case.

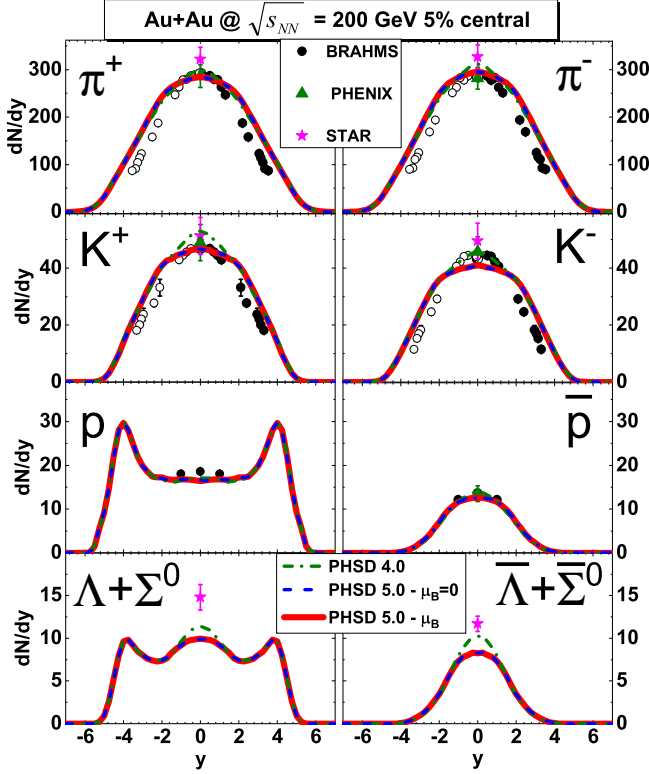


FIG. 23. (Color online) The rapidity distributions for 5% central Au+Au collisions at  $\sqrt{s_{NN}} = 200$  GeV for PHSD4.0 (green dot-dashed lines), PHSD5.0 with partonic cross sections and parton masses calculated for  $\mu_B = 0$  (blue dashed lines) and with cross sections and parton masses evaluated at the actual chemical potential  $\mu_B$  in each individual space-time cell (red lines) in comparison to the experimental data from the BRAHMS [113, 114], PHENIX [115] and STAR [116] collaborations.

This also holds true for the transverse momentum distributions at midrapidity ( $|y| < 0.5$ ) for these collisions when comparing the results from the different PHSD versions with each other and the data from the PHENIX [115] and STAR [116] collaborations in Fig. 24. Only for high transverse momenta small differences can be seen with the tendency to improve the description of the data in the novel versions of PHSD5.0 with the microscopic differential partonic cross sections.

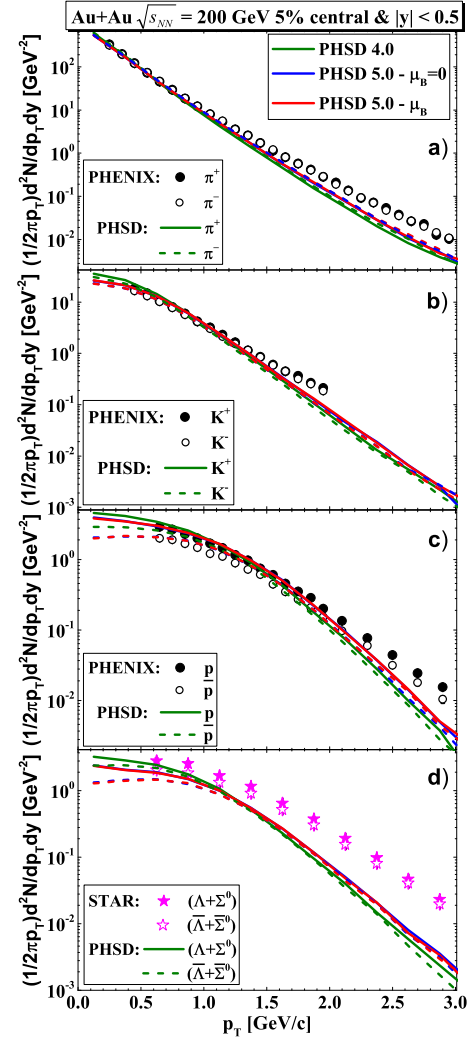


FIG. 24. (Color online) The transverse momentum distributions for 5% central Au+Au collisions at  $\sqrt{s_{NN}} = 200$  GeV and midrapidity ( $|y| < 0.5$ ) for PHSD4.0 (green lines), PHSD5.0 with partonic cross sections and parton masses calculated for  $\mu_B = 0$  (blue lines) and with cross sections and parton masses evaluated at the actual chemical potential  $\mu_B$  in each individual space-time cell (red lines) in comparison to the experimental data from the PHENIX [115] and STAR [116] collaborations.

## C. Asymmetric systems

Since the central collisions of the heavy systems (Au+Au or Pb+Pb) only provide information on the total partonic reaction rate and not on details of the partonic collisional dynamics one has to explore asymmetric heavy-ion collisions - such as C+Au or Cu+Au - in addition in order to find out a possible sensitivity to the partonic collisions. To this end we have performed a systematic study of 5% C+Au and Cu+Au collisions at bombarding energies from AGS to top RHIC energies for the "bulk" observables within the different PHSD versions. We note that (without explicit representation)



we did not find any difference at 10.7 A GeV and 30 A GeV as in case of the heavy symmetric systems for the hadronic rapidity distributions and transverse momentum spectra at midrapidity. For Cu+Au the actual results - w.r.t. to the differences between PHSD4.0 and PHSD5.0 - at all bombarding energies turned out to be very similar to the central Au+Au or Pb+Pb collisions such that an explicit representation is discarded. Only in case of 5% C+Au reactions at top SPS and top RHIC energies some differences have been found which will be discussed in the following.

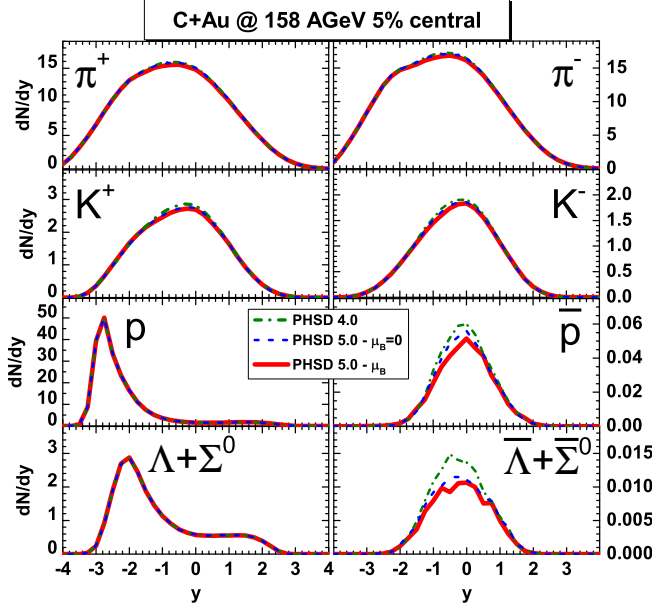


FIG. 25. (Color online) The rapidity distributions for 5% central C+Au collisions at 158 A GeV for PHSD4.0 (green dot-dashed lines), PHSD5.0 with partonic cross sections and parton masses calculated for  $\mu_B = 0$  (blue dashed lines) and with cross sections and parton masses evaluated at the actual chemical potential  $\mu_B$  in each individual space-time cell (red lines).

The rapidity distributions of hadrons for 5% central C+Au collisions are displayed in Figs. 25 and 26 for 158 A GeV and  $\sqrt{s_{NN}} = 200$  GeV, respectively. Note that the rapidity distributions are no longer symmetric in rapidity  $y$  but enhanced for  $y < 0$  (Au-going side). There is no change of the pion and baryon distributions at both energies for the different PHSD versions as in case of the heavy symmetric systems while tiny differences can again be seen in the antibaryon spectra. However, in case of C+Au now there is also a small signal in the kaon rapidity distributions which is more pronounced at  $\sqrt{s_{NN}} = 200$  GeV. This suggests that the strangeness degree of freedom might be explored in very asymmetric systems to obtain additional information on the partonic scattering dynamics.

The transverse momentum spectra of hadrons at midrapidity (for C+Au) are shown in Figs. 27 and 28 for 158 A GeV and  $\sqrt{s_{NN}} = 200$  GeV, respectively. There

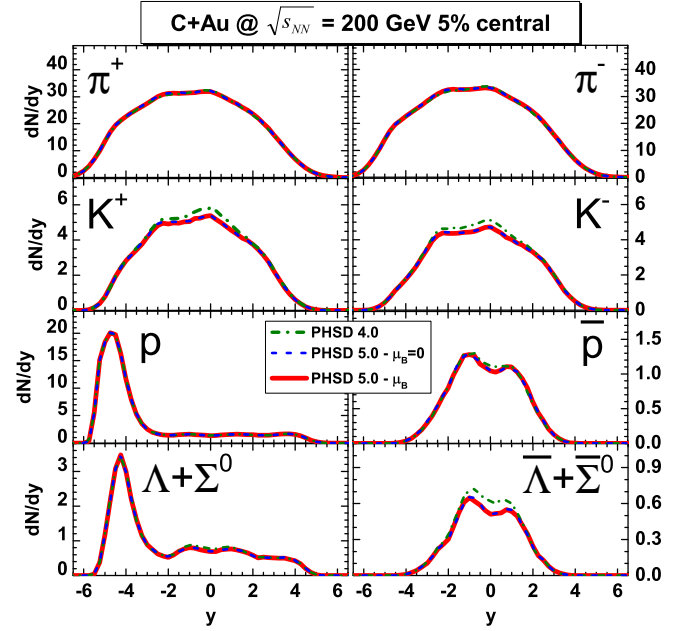


FIG. 26. (Color online) The rapidity distributions for 5% central C+Au collisions at  $\sqrt{s_{NN}} = 200$  GeV for PHSD4.0 (green dot-dashed lines), PHSD5.0 with partonic cross sections and parton masses calculated for  $\mu_B = 0$  (blue dashed lines) and with cross sections and parton masses evaluated at the actual chemical potential  $\mu_B$  in each individual space-time cell (red lines).

is practically no difference in the PHSD4.0 and PHSD5.0 results for pions, kaons, protons and antiprotons and only a very small signal in the antihyperons can be identified. Nevertheless, our results for this very asymmetric system can be considered as predictions for the production of the most abundant hadron species at top SPS and RHIC energies.

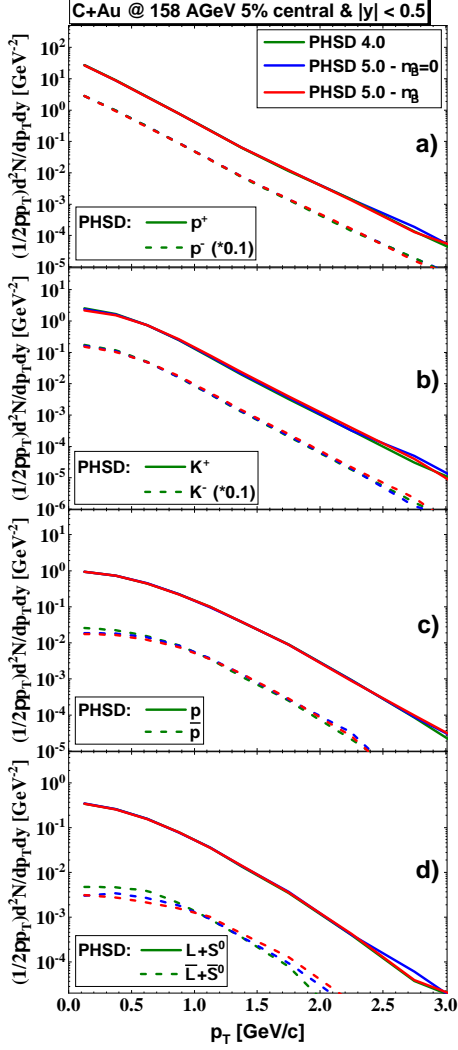


FIG. 27. (Color online) The transverse momentum distributions for 5% central C+Au collisions at 158 A GeV and midrapidity ( $|y| < 0.5$ ) for PHSD4.0 (green lines), PHSD5.0 with partonic cross sections and parton masses calculated for  $\mu_B = 0$  (blue lines) and with cross sections and parton masses evaluated at the actual chemical potential  $\mu_B$  in each individual space-time cell (red lines).

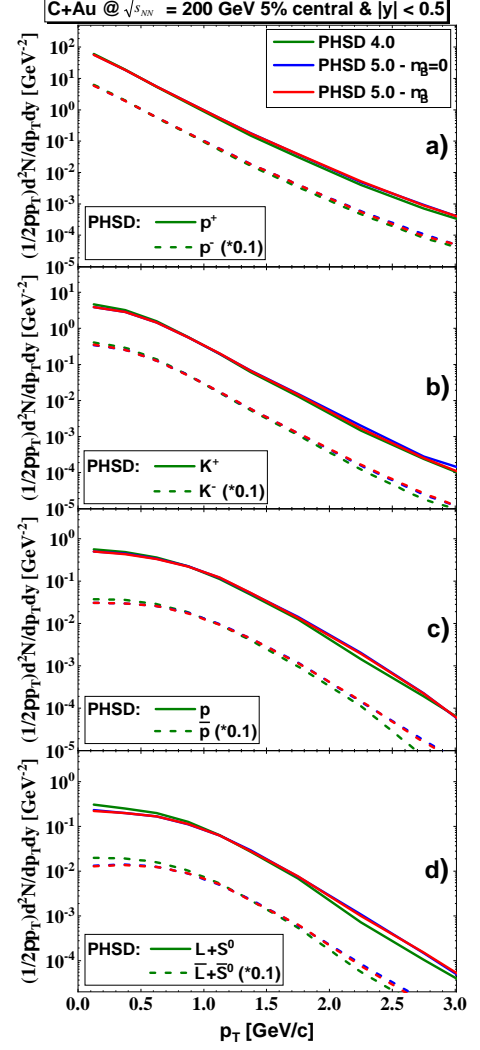


FIG. 28. (Color online) The transverse momentum distributions for 5% central C+Au collisions at  $\sqrt{s_{NN}} = 200$  GeV and midrapidity ( $|y| < 0.5$ ) for PHSD4.0 (green lines), PHSD5.0 with partonic cross sections and parton masses calculated for  $\mu_B = 0$  (blue lines) and with cross sections and parton masses evaluated at the actual chemical potential  $\mu_B$  in each individual space-time cell (red lines).

### VIII. SUMMARY

In this work we have extended the PHSD transport approach (PHSD4.0 [46, 55]) to incorporate differential "off-shell cross sections" for all binary partonic channels that are based on the same effective propagators and couplings as employed in the QGP equation of state and the parton propagation. To this end we have recalled the extraction of the partonic masses and the coupling  $g^2$  from lattice QCD data (within the DQPM) and calculated the partonic differential cross sections as a function of  $T$  and  $\mu_B$  for the leading tree-level diagrams (cf. Appendices). Furthermore, in Section IV we have used these differential cross sections to evaluate partonic scattering rates for fixed  $T$  and  $\mu_B$  as well as to compute the ratio of the shear viscosity  $\eta$  to entropy density  $s$  within the Kubo formalism in comparison to calculations from lQCD. It turns out that the ratio  $\eta/s$  calculated with the partonic scattering rates in the relaxation-time approximation is very similar to the original result from the DQPM and to lQCD results such that the present extension of the approach does not lead to different partonic transport properties except for temperatures close to  $T_c$ . We recall that the novel PHSD version (PHSD5.0) is practically parameter free in the partonic sector since the effective coupling (squared) is determined by a fit to the scaled entropy density from lQCD. The dynamical masses for quarks and gluons then are fixed by the HTL expressions. The interaction rate in the time-like sector is, furthermore, calculated in leading order employing the DQPM propagators and coupling.

When implementing the differential cross sections and parton masses into the PHSD5.0 approach one has to specify the "Lagrange parameters"  $T$  and  $\mu_B$  in each computational cell in space-time. This has been done by employing the DQPM equation of state, which is practically identical to the lattice QCD equation of state (cf. Fig. 3), and a diagonalization of the energy-momentum tensor from PHSD as described in Section V. Detailed results for  $T$  and  $\mu_B$  have been presented for central collisions of Pb+Pb at  $\sqrt{s_{NN}} = 17.3$  and Au+Au 200 GeV in the  $(T, \mu_B)$  plane as a function of reaction time. It turns out that only in the early phase moderate chemical potentials can be found at  $\sqrt{s_{NN}} = 17.3$  with  $T$  above  $T_c$  while at the top RHIC energy the distribution in  $T$  and  $\mu_B$  spreads around zero for all reaction times considered.

In Section VI we then have calculated 5% central Au+Au (or Pb+Pb) collisions and compared the results for hadronic rapidity distributions and transverse momentum spectra (at midrapidity) from the previous PHSD4.0 with the novel version PHSD5.0 (with and without the explicit dependence of the partonic differential cross sections and parton masses on  $\mu_B$ ). No differences for all the hadron "bulk" observables from the various PHSD versions have been found at AGS and FAIR/NICA energies within linewidth which implies that there is no sensitivity to the new partonic differential cross sections employed. Only in case of the kaons and

the antibaryons  $\bar{p}$  and  $\bar{\Lambda} + \bar{\Sigma}^0$ , a small difference between PHSD4.0 and PHSD5.0 could be seen at top SPS and top RHIC energies, however, no clear difference between the PHSD5.0 calculations with partonic cross sections for  $\mu_B = 0$  and actual  $\mu_B$  in the local cells. When considering very asymmetric collisions of C+Au, a small sensitivity to the partonic scatterings was found in the kaon and antibaryon rapidity distributions, too. However, it will be very hard to extract a robust signal experimentally.

Our findings can be understood as follows: The fact that we find only small traces of the  $\mu_B$ -dependence of partonic scattering dynamics in heavy-ion "bulk" observables - although the differential cross sections and parton masses clearly depend on  $\mu_B$  - means that one needs a sizable partonic density and large space-time QGP volume to explore the dynamics in the QGP phase. These conditions are only fulfilled at high bombarding energies (top SPS, RHIC energies) where, however,  $\mu_B$  is rather low. On the other hand, decreasing the bombarding energy to FAIR/NICA energies and, thus, increasing  $\mu_B$ , leads to collisions that are dominated by the hadronic phase where the extraction of information about the parton dynamics will be rather complicated based on "bulk" observables. Further investigations of other observables (such as flow coefficients  $v_n$  of particles and antiparticles, fluctuations and correlations) might contain more visible " $\mu_B$ -traces" from the QGP phase.

### ACKNOWLEDGEMENTS

The authors acknowledge inspiring discussions with J. Aichelin, H. Berrehrah, C. Ratti and T. Steinert. This work was supported by the LOEWE center "HIC for FAIR". Furthermore, P.M., L.O. and E.B. acknowledge support by the Deutsche Forschungsgemeinschaft (DFG, German Research Foundation) through the grant CRC-TR 211 'Strong-interaction matter under extreme conditions' - Project number 315477589 - TRR 211. O.S. acknowledges support from HGS-HiRe for FAIR; L.O. and E.B. thank the COST Action THOR, CA15213. The computational resources have been provided by the LOEWE-Center for Scientific Computing.

## APPENDIX

In this Appendix we give the details on the calculation of the matrix elements used to evaluate the DQPM partonic cross sections which are based on Refs. [66, 117, 118]. We recall that the Mandelstam variables are given by the momenta as  $s = (k_i + p_i)^2 = (k_f + p_f)^2$ ,  $t = (k_i - k_f)^2 = (p_i - p_f)^2$ ,  $u = (k_i - p_f)^2 = (p_i - k_f)^2$ . The generators of  $SU(3)$  associated with QCD are denoted by the matrices  $T^a = \lambda^a/2$  with  $a$  being the gluon color and  $\lambda^a$  the Gell-Mann matrices [119]. The Lie algebra formed by the generators  $T^a$  is given by the commutation relation  $[T^a, T^b] = if^{abc}T^c$  where  $f^{abc}$  are the structure constants. We refer the reader to Ref. [120] where all the rules for calculating the color factors in the following calculations are given in detail. The gamma matrices are denoted by  $\gamma^\mu$  and the Dirac spinors are  $u$  for particles and  $v$  for antiparticles. The final analytical expressions for the matrix elements used in the PHSD code were evaluated using FeynCalc [121, 122].

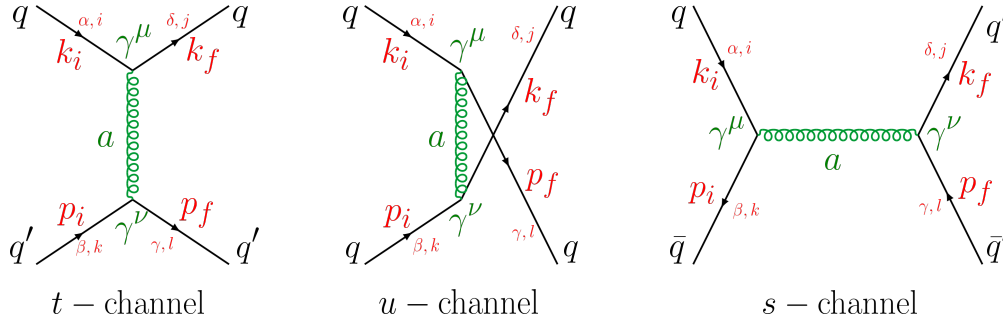
Appendix A: Matrix elements for  $qq' \rightarrow qq'$  scattering

FIG. 29. Leading order Feynman diagrams for the  $qq' \rightarrow qq'$  and  $q\bar{q} \rightarrow q'\bar{q}'$  processes. The initial and final 4-momenta are  $k_i$  and  $p_i$ , and  $k_f$  and  $p_f$ , respectively. The indices  $i, j, k, l = 1 - 3$  denote the quark colors,  $a = 1 - 8$  the gluon colors while the quark flavor is indicated by the indices  $\alpha, \beta, \delta, \gamma = u, d, s, \dots$

The invariant matrix elements corresponding to Fig. 29 are given by the following expressions:

$$i\mathcal{M}_t(q_\alpha^i q_\beta^k \rightarrow q_\delta^j q_\gamma^l) = \delta_{\alpha\delta} \delta_{\beta\gamma} \bar{u}_\delta^j(k_f) (-ig\gamma^\mu T_{ij}^a) u_\alpha^i(k_i) \left[ -i \frac{g_{\mu\nu} - (q_\mu^t q_\nu^t)/M_g^2}{(k_f - k_i)^2 - M_g^2 + 2i\gamma_g \omega_t} \right] \bar{u}_\gamma^l(p_f) (-ig\gamma^\nu T_{kl}^a) u_\beta^k(p_i), \quad (\text{A1})$$

$$i\mathcal{M}_u(q_\alpha^i q_\beta^k \rightarrow q_\delta^j q_\gamma^l) = -\delta_{\alpha\beta} \delta_{\alpha\delta} \delta_{\beta\gamma} \bar{u}_\delta^j(k_f) (-ig\gamma^\nu T_{kj}^a) u_\beta^k(p_i) \left[ -i \frac{g_{\mu\nu} - (q_\mu^u q_\nu^u)/M_g^2}{(p_f - k_i)^2 - M_g^2 + 2i\gamma_g \omega_u} \right] \bar{u}_\gamma^l(p_f) (-ig\gamma^\mu T_{il}^a) u_\alpha^i(k_i), \quad (\text{A2})$$

$$i\mathcal{M}_s(q_\alpha^i q_\beta^k \rightarrow q_\delta^j q_\gamma^l) = -\delta_{\alpha\bar{\beta}} \delta_{\delta\bar{\gamma}} \bar{u}_\delta^j(k_f) (-ig\gamma^\nu T_{lj}^a) v_\gamma^l(p_f) \left[ -i \frac{g_{\mu\nu} - (q_\mu^s q_\nu^s)/M_g^2}{(k_i + p_i)^2 - M_g^2 + 2i\gamma_g \omega_s} \right] \bar{v}_\beta^k(p_i) (-ig\gamma^\mu T_{ik}^a) u_\alpha^i(k_i), \quad (\text{A3})$$

where the energy of the exchanged gluon is  $\omega_t = |k_f^0 - k_i^0|$ ,  $\omega_u = |p_f^0 - k_i^0|$  and  $\omega_s = |k_i^0 + p_i^0|$ , and its momentum denoted by  $q_t^\mu = (k_f - k_i)^\mu$ ,  $q_u^\mu = (p_i - k_f)^\mu$  and  $q_s^\mu = (k_i + p_i)^\mu$ . We note here that the matrix element  $\mathcal{M}_t$  given above only corresponds to a  $q - q$  elastic scattering, but the final contribution from  $t$ -channel diagrams to  $|\bar{\mathcal{M}}|^2$  is found to be the same whether a quark scatters with a quark or antiquark since the amplitudes are averaged (summed) over initial (final) partons as:

$$\begin{aligned} |\bar{\mathcal{M}}(q_\alpha q_\beta \rightarrow q_\delta q_\gamma)|^2 &= \frac{1}{d_q^2} \sum_{\text{color}} \sum_{\text{spin}} |\mathcal{M}_t + \mathcal{M}_u + \mathcal{M}_s|^2 \\ &= \frac{1}{3 \times 3} \sum_{\text{color}} \frac{1}{2 \times 2} \sum_{\text{spin}} (|\mathcal{M}_t|^2 + |\mathcal{M}_u|^2 + |\mathcal{M}_s|^2 + 2 \text{Re}[\mathcal{M}_t \mathcal{M}_u^*] + 2 \text{Re}[\mathcal{M}_t \mathcal{M}_s^*] + 2 \text{Re}[\mathcal{M}_u \mathcal{M}_s^*]). \end{aligned} \quad (\text{A4})$$

### Appendix B: Matrix elements for $gq \rightarrow gq$ scattering

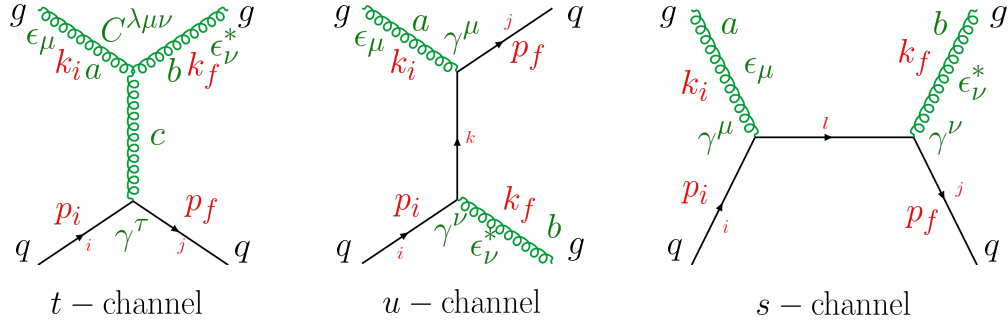


FIG. 30. Leading order Feynman diagrams for the  $gq \rightarrow gq$  processes. The initial and final 4-momenta are  $k_i$  and  $p_i$ , and  $k_f$  and  $p_f$ , respectively. The indices  $i, j, k, l = 1-3$  denote the quark colors,  $a, b, c = 1-8$  the gluon colors while the quark flavor is indicated by the indices  $\alpha, \beta, \delta, \gamma = u, d, s, \dots$

The invariant matrix elements corresponding to the Feynman diagrams in Fig. 30 are given by the following expressions:

$$i\mathcal{M}_t(g^a q^i \rightarrow g^b q^j) = (\epsilon_{b,f}^*)_\nu (-gf^{cab} C^{\lambda\mu\nu}(k_i - k_f, -k_i, k_f)) (\epsilon_{a,i})_\mu \left[ -i \frac{g_{\lambda\tau} - (q_\lambda^t q_\tau^t)/M_g^2}{(k_f - k_i)^2 - M_g^2 + 2i\gamma_g \omega_t} \right] \bar{u}^j(p_f) (-ig\gamma^\tau T_{ij}^c) u^i(p_i), \quad (\text{B1})$$

$$i\mathcal{M}_u(g^a q^i \rightarrow g^b q^j) = \bar{u}^j(p_f) (-ig\gamma^\mu T_{kj}^a) (\epsilon_{a,i})_\mu \left[ i \frac{\not{k}^u + M_q}{u - M_q^2 + 2i\gamma_q \omega_u} \right] (\epsilon_{b,f}^*)_\nu (-ig\gamma^\nu T_{ik}^b) u^i(p_i), \quad (\text{B2})$$

$$i\mathcal{M}_s(g^a q^i \rightarrow g^b q^j) = \bar{u}^j(p_f) (-ig\gamma^\nu T_{lj}^b) (\epsilon_{b,f}^*)_\nu \left[ i \frac{\not{k}^s + M_q}{s - M_q^2 + 2i\gamma_q \omega_s} \right] (\epsilon_{a,i})_\mu (-ig\gamma^\mu T_{il}^a) u^i(p_i). \quad (\text{B3})$$

with the 3-gluon vertex  $C^{\lambda\mu\nu}(q_1, q_2, q_3) = [(q_1 - q_2)^\nu g^{\lambda\mu} + (q_2 - q_3)^\lambda g^{\mu\nu} + (q_3 - q_1)^\mu g^{\lambda\nu}]$  and the momentum of the exchanged gluon  $q_t^\mu = (k_f - k_i)^\mu$  in the  $t$ -channel.

In the case of a massive gluon, the sum over polarizations is given by (in accordance with the denominator of the propagator in Eq. (27)):

$$\sum_{\text{pol.}} (\epsilon_i)_\mu (\epsilon_i^*)_{\mu'} = -g_{\mu\mu'} + \frac{(k_i)_\mu (k_i)_{\mu'}}{(M_i)^2}, \quad (\text{B4})$$

The invariant matrix element squared averaged (summed) over the initial (final) partons is:

$$\begin{aligned} |\overline{\mathcal{M}}(gq \rightarrow gq)|^2 &= \frac{1}{d_g d_q} \sum_{\text{color}} \sum_{\text{spin}} |\mathcal{M}_t + \mathcal{M}_u + \mathcal{M}_s|^2 \\ &= \frac{1}{8 \times 3} \sum_{\text{color}} \frac{1}{2 \times 2} \sum_{\text{spin}} (|\mathcal{M}_t|^2 + |\mathcal{M}_u|^2 + |\mathcal{M}_s|^2 + 2 \text{Re} [\mathcal{M}_t \mathcal{M}_u^*] + 2 \text{Re} [\mathcal{M}_t \mathcal{M}_s^*] + 2 \text{Re} [\mathcal{M}_u \mathcal{M}_s^*]). \end{aligned} \quad (\text{B5})$$

### Appendix C: Matrix elements for $gg \rightarrow gg$ scattering

The invariant matrix elements corresponding to the Feynman diagrams in Fig. 31 are given by the following expressions:



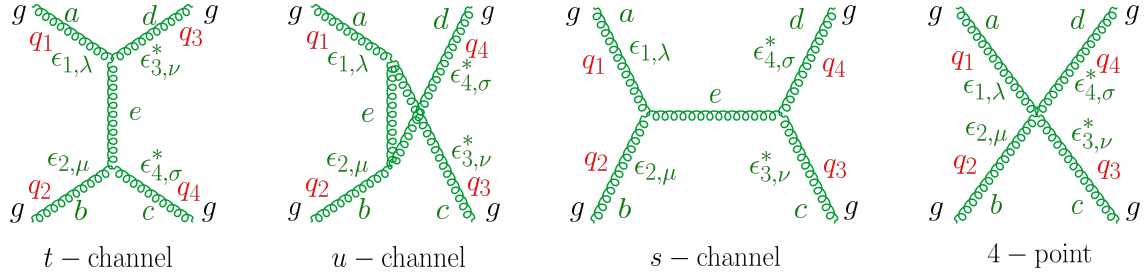


FIG. 31. Leading order Feynman diagrams for the  $gg \rightarrow gg$  scatterings. The initial and final 4-momenta are  $k_i$  and  $p_i$ , and  $k_f$  and  $p_f$ , respectively. The indices  $a, b, c, d, e = 1 - 8$  denote the gluon colors.

$$i\mathcal{M}_t(g^a g^b \rightarrow g^c g^d) = (\epsilon_{d,4}^*)_\sigma \left( -gf^{ead} C^{\tau\lambda\sigma}(q_1 - q_4, -q_1, q_4) \right) (\epsilon_{a,1})_\lambda$$

$$\left[ -i \frac{g_{\tau\tau'} - (q_\tau^t q_{\tau'}^t)/M_g^2}{(q_4 - q_1)^2 - M_g^2 + 2i\gamma_g \omega_t} \right] (\epsilon_{c,3}^*)_\nu \left( -gf^{ecb} C^{\tau'\nu\mu}(-q_3 + q_2, q_3, -q_2) \right) (\epsilon_{b,2})_\mu, \quad (\text{C1})$$

$$i\mathcal{M}_s(g^a g^b \rightarrow g^c g^d) = (\epsilon_{d,4}^*)_\sigma \left( -gf^{edc} C^{\tau'\sigma\nu}(-q_4 - q_3, q_4, q_3) \right) (\epsilon_{c,3}^*)_\nu$$

$$\left[ -i \frac{g_{\tau\tau'} - (q_\tau^s q_{\tau'}^s)/M_g^2}{(q_1 + q_2)^2 - M_g^2 + 2i\gamma_g \omega_s} \right] (\epsilon_{b,2})_\mu \left( -gf^{eba} C^{\tau\mu\lambda}(q_2 + q_1, -q_2, -q_1) \right) (\epsilon_{a,1})_\lambda \quad (\text{C2})$$

$$i\mathcal{M}_u(g^a g^b \rightarrow g^c g^d) = (\epsilon_{d,4}^*)_\sigma \left( -gf^{edb} C^{\tau'\sigma\mu}(-q_4 + q_2, q_4, -q_2) \right) (\epsilon_{b,2})_\mu$$

$$\left[ -i \frac{g_{\tau\tau'} - (q_\tau^u q_{\tau'}^u)/M_g^2}{(q_2 - q_4)^2 - M_g^2 + 2i\gamma_g \omega_u} \right] (\epsilon_{c,3}^*)_\nu \left( -gf^{eac} C^{\tau\lambda\nu}(q_1 - q_3, -q_1, q_3) \right) (\epsilon_{a,1})_\lambda, \quad (\text{C3})$$

with the 3-gluon vertex  $C^{\lambda\mu\nu}(q_1, q_2, q_3) = [(q_1 - q_2)^\nu g^{\lambda\mu} + (q_2 - q_3)^\lambda g^{\mu\nu} + (q_3 - q_1)^\mu g^{\lambda\nu}]$  and the momentum of the exchanged gluon  $q_t^\mu = (q_4 - q_1)^\mu$ ,  $q_s^\mu = (q_1 + q_2)^\mu$  and  $q_u^\mu = (q_2 - q_4)^\mu$ .

The 4-point invariant amplitude is given by (according to Refs. [117, 118]):

$$i\mathcal{M}_4(g^a g^b \rightarrow g^c g^d) = -ig^2 [f^{abe} f^{cde} (g^{\lambda\nu} g^{\mu\sigma} - g^{\lambda\sigma} g^{\mu\nu}) + f^{ace} f^{bde} (g^{\lambda\mu} g^{\nu\sigma} - g^{\lambda\sigma} g^{\nu\mu})$$

$$+ f^{ade} f^{cbe} (g^{\lambda\mu} g^{\sigma\nu} - g^{\lambda\nu} g^{\sigma\mu})] (\epsilon_{d,4}^*)_\sigma (\epsilon_{c,3}^*)_\nu (\epsilon_{b,2})_\mu (\epsilon_{a,1})_\lambda,$$

$$\mathcal{M}_4(g^a g^b \rightarrow g^c g^d) = f^{abe} f^{cde} \mathcal{M}_4^s + f^{ace} f^{bde} \mathcal{M}_4^u + f^{ade} f^{cbe} \mathcal{M}_4^t. \quad (\text{C4})$$

The invariant matrix element squared averaged (summed) over the initial (final) gluons is:

$$|\overline{\mathcal{M}}(gg \rightarrow gg)|^2 = \frac{1}{d_g^2} \sum_{\text{color}} \sum_{\text{spin}} |\mathcal{M}(g^a g^b \rightarrow g^c g^d)|^2 \quad (\text{C5})$$

$$= \frac{1}{8 \times 8} \sum_{\text{color}} \frac{1}{2 \times 2} \sum_{\text{spin}} (|\mathcal{M}_t|^2 + |\mathcal{M}_s|^2 + |\mathcal{M}_u|^2 + |\mathcal{M}_4|^2 + 2 \text{Re} [\mathcal{M}_t \mathcal{M}_s^*] + 2 \text{Re} [\mathcal{M}_t \mathcal{M}_u^*]$$

$$+ 2 \text{Re} [\mathcal{M}_u \mathcal{M}_s^*] + 2 \text{Re} [\mathcal{M}_t \mathcal{M}_4^*] + 2 \text{Re} [\mathcal{M}_s \mathcal{M}_4^*] + 2 \text{Re} [\mathcal{M}_u \mathcal{M}_4^*]).$$

- 4, 12 (1963).
- [3] L. V. Keldysh, Zh. Eksp. Teor. Fiz. **47**, 1515 (1964), [Sov. Phys. JETP20,1018(1965)].
  - [4] R. A. Craig, *Journal of Mathematical Physics* **9**, 605 (1968), <https://doi.org/10.1063/1.1664616>.
  - [5] M. Bonitz, *Quantum Kinetic Theory*, Teubner Texte zur Physik (Vieweg+Teubner Verlag, 1998).
  - [6] L. P. Kadanoff and G. Baym, *Quantum Statistical mechanics* (W. A. Benjamin, Inc., New York, 1962).
  - [7] D. DuBois, *Quantum Kinetics in Transport and Optics of Semiconductors* (edited by W. E. Brittin (Gordon and Breach, NY 1967) pp 469-619).
  - [8] P. Danielewicz, *Annals Phys.* **152**, 305 (1984).
  - [9] K.-c. Chou, Z.-b. Su, B.-l. Hao, and L. Yu, *Phys. Rept.* **118**, 1 (1985).
  - [10] J. Rammer and H. Smith, *Rev. Mod. Phys.* **58**, 323 (1986).
  - [11] E. Calzetta and B. L. Hu, *Phys. Rev.* **D37**, 2878 (1988).
  - [12] H. Haug and A. Jauho, *Quantum Kinetics in Transport and Optics of Semiconductors*, Springer Series in Solid-State Sciences (Springer Berlin Heidelberg, 1998).
  - [13] B. Bezzerides and D. DuBois, *Annals of Physics* **70**, 10 (1972).
  - [14] W. Botermans and R. Malfliet, *Phys. Rept.* **198**, 115 (1990).
  - [15] S. Mrowczynski and P. Danielewicz, *Nucl. Phys.* **B342**, 345 (1990).
  - [16] A. Makhlin and E. Surdutovich, *Phys. Rev.* **C58**, 389 (1998), [arXiv:hep-ph/9803364](https://arxiv.org/abs/hep-ph/9803364) [hep-ph].
  - [17] A. Makhlin, *Phys. Rev.* **C52**, 995 (1995), [arXiv:hep-ph/9412363](https://arxiv.org/abs/hep-ph/9412363) [hep-ph].
  - [18] K. Geiger, *Phys. Rev.* **D54**, 949 (1996), [arXiv:hep-ph/9507365](https://arxiv.org/abs/hep-ph/9507365) [hep-ph].
  - [19] K. Geiger, *Phys. Rev.* **D56**, 2665 (1997), [arXiv:hep-ph/9611400](https://arxiv.org/abs/hep-ph/9611400) [hep-ph].
  - [20] D. A. Brown and P. Danielewicz, *Phys. Rev.* **D58**, 094003 (1998), [arXiv:nucl-th/9802015](https://arxiv.org/abs/nucl-th/9802015) [nucl-th].
  - [21] J.-P. Blaizot and E. Iancu, *Nucl. Phys.* **B557**, 183 (1999), [arXiv:hep-ph/9903389](https://arxiv.org/abs/hep-ph/9903389) [hep-ph].
  - [22] W. Cassing and S. Juchem, *Nucl. Phys.* **A665**, 377 (2000), [arXiv:nucl-th/9903070](https://arxiv.org/abs/nucl-th/9903070) [nucl-th].
  - [23] W. Cassing and S. Juchem, *Nucl. Phys.* **A672**, 417 (2000), [arXiv:nucl-th/9910052](https://arxiv.org/abs/nucl-th/9910052) [nucl-th].
  - [24] Yu. B. Ivanov, J. Knoll, and D. N. Voskresensky, *Nucl. Phys.* **A657**, 413 (1999), [arXiv:hep-ph/9807351](https://arxiv.org/abs/hep-ph/9807351) [hep-ph].
  - [25] J. Knoll, Yu. B. Ivanov, and D. N. Voskresensky, *Annals Phys.* **293**, 126 (2001), [arXiv:nucl-th/0102044](https://arxiv.org/abs/nucl-th/0102044) [nucl-th].
  - [26] W. Cassing, *Eur. Phys. J. ST* **168**, 3 (2009), [arXiv:0808.0715](https://arxiv.org/abs/0808.0715) [nucl-th].
  - [27] H. A. Weldon, *Phys. Rev.* **D28**, 2007 (1983).
  - [28] V. V. Lebedev and A. V. Smilga, *Annals Phys.* **202**, 229 (1990).
  - [29] E. Braaten and R. D. Pisarski, *Phys. Rev.* **D42**, 2156 (1990).
  - [30] E. Braaten and R. D. Pisarski, *Phys. Rev.* **D46**, 1829 (1992).
  - [31] R. D. Pisarski, *Phys. Rev.* **D47**, 5589 (1993).
  - [32] S. Jeon, *Phys. Rev.* **D52**, 3591 (1995), [arXiv:hep-ph/9409250](https://arxiv.org/abs/hep-ph/9409250) [hep-ph].
  - [33] E.-k. Wang and U. W. Heinz, *Phys. Rev.* **D53**, 899 (1996), [arXiv:hep-ph/9509333](https://arxiv.org/abs/hep-ph/9509333) [hep-ph].
  - [34] M. H. Thoma, *Phys. Rev.* **D49**, 451 (1994), [arXiv:hep-ph/9308257](https://arxiv.org/abs/hep-ph/9308257) [hep-ph].
  - [35] S. Y. F. Liu and R. Rapp, *Phys. Rev.* **C97**, 034918 (2018), [arXiv:1711.03282](https://arxiv.org/abs/1711.03282) [nucl-th].
  - [36] B. Vanderheyden and G. Baym, *J. Stat. Phys.* (1998), 10.1023/B:JOSS.0000033166.37520.ae, [*J. Statist. Phys.*93,843(1998)], [arXiv:hep-ph/9803300](https://arxiv.org/abs/hep-ph/9803300) [hep-ph].
  - [37] C. Bernard, T. Burch, E. B. Gregory, D. Toussaint, C. E. DeTar, J. Osborn, S. Gottlieb, U. M. Heller, and R. Sugar (MILC), *Phys. Rev.* **D71**, 034504 (2005), [arXiv:hep-lat/0405029](https://arxiv.org/abs/hep-lat/0405029) [hep-lat].
  - [38] Y. Aoki, G. Endrodi, Z. Fodor, S. D. Katz, and K. K. Szabo, *Nature* **443**, 675 (2006), [arXiv:hep-lat/0611014](https://arxiv.org/abs/hep-lat/0611014) [hep-lat].
  - [39] A. Bazavov *et al.*, *Phys. Rev.* **D85**, 054503 (2012), [arXiv:1111.1710](https://arxiv.org/abs/1111.1710) [hep-lat].
  - [40] C. S. Fischer and J. Luecker, *Phys. Lett.* **B718**, 1036 (2013), [arXiv:1206.5191](https://arxiv.org/abs/1206.5191) [hep-ph].
  - [41] C. S. Fischer, (2018), [arXiv:1810.12938](https://arxiv.org/abs/1810.12938) [hep-ph].
  - [42] P. Senger, E. Bratkovskaya, A. Andronic, R. Averbeck, R. Bellwied, V. Friese, C. Fuchs, J. Knoll, J. Randrup, and J. Steinheimer, *Lect. Notes Phys.* **814**, 681 (2011).
  - [43] B. Mohanty (STAR), *J. Phys.* **G38**, 124023 (2011), [arXiv:1106.5902](https://arxiv.org/abs/1106.5902) [nucl-ex].
  - [44] L. Kumar (STAR), *J. Phys.* **G38**, 124145 (2011), [arXiv:1106.6071](https://arxiv.org/abs/1106.6071) [nucl-ex].
  - [45] W. Cassing, A. Palmese, P. Moreau, and E. L. Bratkovskaya, *Phys. Rev.* **C93**, 014902 (2016), [arXiv:1510.04120](https://arxiv.org/abs/1510.04120) [nucl-th].
  - [46] A. Palmese, W. Cassing, E. Seifert, T. Steinert, P. Moreau, and E. L. Bratkovskaya, *Phys. Rev.* **C94**, 044912 (2016), [arXiv:1607.04073](https://arxiv.org/abs/1607.04073) [nucl-th].
  - [47] C. Shen and B. Schenke, *Proceedings, 27th International Conference on Ultrarelativistic Nucleus-Nucleus Collisions (Quark Matter 2018): Venice, Italy, May 14-19, 2018*, *Nucl. Phys.* **A982**, 411 (2019), [arXiv:1807.05141](https://arxiv.org/abs/1807.05141) [nucl-th].
  - [48] M. Li and C. Shen, *Phys. Rev.* **C98**, 064908 (2018), [arXiv:1809.04034](https://arxiv.org/abs/1809.04034) [nucl-th].
  - [49] Yu. B. Ivanov, V. N. Russkikh, and V. D. Toneev, *Phys. Rev.* **C73**, 044904 (2006), [arXiv:nucl-th/0503088](https://arxiv.org/abs/nucl-th/0503088) [nucl-th].
  - [50] Yu. B. Ivanov and D. Blaschke, *Phys. Rev.* **C92**, 024916 (2015), [arXiv:1504.03992](https://arxiv.org/abs/1504.03992) [nucl-th].
  - [51] G. S. Denicol, C. Gale, S. Jeon, A. Monnai, B. Schenke, and C. Shen, *Phys. Rev.* **C98**, 034916 (2018), [arXiv:1804.10557](https://arxiv.org/abs/1804.10557) [nucl-th].
  - [52] H. Petersen, J. Steinheimer, G. Burau, M. Bleicher, and H. Stocker, *Phys. Rev.* **C78**, 044901 (2008), [arXiv:0806.1695](https://arxiv.org/abs/0806.1695) [nucl-th].
  - [53] M. Li and J. I. Kapusta, *Phys. Rev.* **C99**, 014906 (2019), [arXiv:1808.05751](https://arxiv.org/abs/1808.05751) [nucl-th].
  - [54] W. Cassing and E. L. Bratkovskaya, *Nucl. Phys.* **A831**, 215 (2009), [arXiv:0907.5331](https://arxiv.org/abs/0907.5331) [nucl-th].
  - [55] O. Linnyk, E. L. Bratkovskaya, and W. Cassing, *Prog. Part. Nucl. Phys.* **87**, 50 (2016), [arXiv:1512.08126](https://arxiv.org/abs/1512.08126) [nucl-th].
  - [56] V. Ozvenchuk, O. Linnyk, M. I. Gorenstein, E. L. Bratkovskaya, and W. Cassing, *Phys. Rev.* **C87**, 024901 (2013), [arXiv:1203.4734](https://arxiv.org/abs/1203.4734) [nucl-th].
  - [57] O. Linnyk, W. Cassing, J. Manninen, E. L. Bratkovskaya, P. B. Gossiaux, J. Aichelin, T. Song, and C. M. Ko, *Phys. Rev.* **C87**, 014905 (2013), [arXiv:1208.1279](https://arxiv.org/abs/1208.1279) [nucl-th].
  - [58] E. L. Bratkovskaya, W. Cassing, V. P. Konchakovski, and O. Linnyk, *Nucl. Phys.* **A856**, 162 (2011),

- arXiv:1101.5793 [nucl-th].
- [59] V. P. Konchakovski, W. Cassing, and V. D. Toneev, *J. Phys.* **G42**, 055106 (2015), arXiv:1411.5534 [nucl-th].
- [60] V. P. Konchakovski, E. L. Bratkovskaya, W. Cassing, V. D. Toneev, and V. Voronyuk, *Phys. Rev.* **C85**, 011902 (2012), arXiv:1109.3039 [nucl-th].
- [61] V. P. Konchakovski, E. L. Bratkovskaya, W. Cassing, V. D. Toneev, S. A. Voloshin, and V. Voronyuk, *Phys. Rev.* **C85**, 044922 (2012), arXiv:1201.3320 [nucl-th].
- [62] V. P. Konchakovski, W. Cassing, Yu. B. Ivanov, and V. D. Toneev, *Phys. Rev.* **C90**, 014903 (2014), arXiv:1404.2765 [nucl-th].
- [63] H. Berrehrah, W. Cassing, E. Bratkovskaya, and T. Steinert, *Phys. Rev.* **C93**, 044914 (2016), arXiv:1512.06909 [hep-ph].
- [64] H. Berrehrah, E. Bratkovskaya, T. Steinert, and W. Cassing, *Int. J. Mod. Phys.* **E25**, 1642003 (2016), arXiv:1605.02371 [hep-ph].
- [65] S. S. Adler *et al.* (PHENIX), *Phys. Rev. Lett.* **91**, 182301 (2003), arXiv:nucl-ex/0305013 [nucl-ex].
- [66] H. Berrehrah, E. Bratkovskaya, W. Cassing, P. B. Gosiaux, J. Aichelin, and M. Bleicher, *Phys. Rev.* **C89**, 054901 (2014), arXiv:1308.5148 [hep-ph].
- [67] H. Berrehrah, E. Bratkovskaya, W. Cassing, and R. Marty, *J. Phys. Conf. Ser.* **612**, 012050 (2015), arXiv:1412.1017 [hep-ph].
- [68] H. Berrehrah, E. Bratkovskaya, W. Cassing, P. B. Gosiaux, and J. Aichelin, *Phys. Rev.* **C91**, 054902 (2015), arXiv:1502.01700 [hep-ph].
- [69] O. Kaczmarek, F. Karsch, F. Zantow, and P. Petreczky, *Phys. Rev.* **D70**, 074505 (2004), [Erratum: *Phys. Rev.* **D72**, 059903 (2005)], arXiv:hep-lat/0406036 [hep-lat].
- [70] S. Borsanyi, G. Endrodi, Z. Fodor, S. D. Katz, S. Krieg, C. Ratti, and K. K. Szabo, *JHEP* **08**, 053 (2012), arXiv:1204.6710 [hep-lat].
- [71] S. Borsanyi, Z. Fodor, C. Hoelbling, S. D. Katz, S. Krieg, and K. K. Szabo, *Phys. Lett.* **B730**, 99 (2014), arXiv:1309.5258 [hep-lat].
- [72] F. Karsch, *PoS CPOD2013*, 046 (2013), arXiv:1307.3978 [hep-ph].
- [73] A. Bazavov *et al.*, *Phys. Rev.* **D95**, 054504 (2017), arXiv:1701.04325 [hep-lat].
- [74] T. Steinert and W. Cassing, *Proceedings, 5th FAIR NExt generation ScientistS (FAIRNESS 2017): Sitges, Barcelona, Spain, May 28-June 3, 2018*, *J. Phys. Conf. Ser.* **1024**, 012029 (2018).
- [75] L. Adamczyk *et al.* (STAR), *Phys. Rev.* **C96**, 044904 (2017), arXiv:1701.07065 [nucl-ex].
- [76] R. D. Pisarski, *Physica A158 (1989) 146-157*, *Physica* **A158**, 146 (1989).
- [77] J. P. Blaizot, E. Iancu, and A. Rebhan, *Phys. Rev.* **D63**, 065003 (2001), arXiv:hep-ph/0005003 [hep-ph].
- [78] L. Rauber and W. Cassing, *Phys. Rev.* **D89**, 065008 (2014), arXiv:1401.5381 [nucl-th].
- [79] E. Braaten and M. H. Thoma, *Phys. Rev.* **D44**, 1298 (1991).
- [80] P. Chakraborty and J. I. Kapusta, *Phys. Rev.* **C83**, 014906 (2011), arXiv:1006.0257 [nucl-th].
- [81] R. Kubo, *J. Phys. Soc. Jap.* **12**, 570 (1957).
- [82] D. Zubarev, V. Morozov, and G. Röpke, *Statistical Mechanics of Nonequilibrium Processes: Relaxation and hydrodynamic processes*, Statistical Mechanics of Nonequilibrium Processes (Akademie Verlag, 1996).
- [83] V. Ozvenchuk, O. Linnyk, M. I. Gorenstein, E. L. Bratkovskaya, and W. Cassing, *Phys. Rev.* **C87**, 064903 (2013), arXiv:1212.5393 [hep-ph].
- [84] G. Aarts and J. M. Martinez Resco, *JHEP* **04**, 053 (2002), arXiv:hep-ph/0203177 [hep-ph].
- [85] M. Iwasaki, H. Ohnishi, and T. Fukutome, *J. Phys.* **G35**, 035003 (2008), arXiv:hep-ph/0703271 [hep-ph].
- [86] R. Lang, N. Kaiser, and W. Weise, *Eur. Phys. J.* **A48**, 109 (2012), arXiv:1205.6648 [hep-ph].
- [87] R. Lang and W. Weise, *Eur. Phys. J.* **A50**, 63 (2014), arXiv:1311.4628 [hep-ph].
- [88] M. Albright and J. I. Kapusta, *Phys. Rev.* **C93**, 014903 (2016), arXiv:1508.02696 [nucl-th].
- [89] J.-P. Blaizot and E. Iancu, *Nucl. Phys.* **B557**, 183 (1999), arXiv:hep-ph/9903389 [hep-ph].
- [90] G. Policastro, D. T. Son, and A. O. Starinets, *Phys. Rev. Lett.* **87**, 081601 (2001), arXiv:hep-th/0104066 [hep-th].
- [91] P. Kovtun, D. T. Son, and A. O. Starinets, *Phys. Rev. Lett.* **94**, 111601 (2005), arXiv:hep-th/0405231 [hep-th].
- [92] N. Astrakhantsev, V. Braguta, and A. Kotov, *JHEP* **04**, 101 (2017), arXiv:1701.02266 [hep-lat].
- [93] Y. Xu, P. Moreau, T. Song, M. Nahrgang, S. A. Bass, and E. Bratkovskaya, *Phys. Rev.* **C96**, 024902 (2017), arXiv:1703.09178 [nucl-th].
- [94] R. Ryblewski and W. Florkowski, *Phys. Rev.* **C85**, 064901 (2012), arXiv:1204.2624 [nucl-th].
- [95] I. Newton and J. Colson, *The Method of Fluxions and Infinite Series;: With Its Application to the Geometry of Curve-Lines* (London:: Printed by Henry Woodfall; and sold by John Nourse, 1736).
- [96] J. Raphson, *Analysis aequationum universalis seu ad aequationes algebraicas resolvendas methodus generalis, & expedita, ex nova infinitarum serierum methodo, deducta ac demonstrata* (1967).
- [97] J. Günther, R. Bellwied, S. Borsanyi, Z. Fodor, S. D. Katz, A. Pasztor, and C. Ratti, *Proceedings, 12th Conference on Quark Confinement and the Hadron Spectrum (Confinement XII): Thessaloniki, Greece, EPJ Web Conf.* **137**, 07008 (2017).
- [98] W. Cassing and E. L. Bratkovskaya, *Phys. Rept.* **308**, 65 (1999).
- [99] Y. Akiba *et al.* (E802), *Nucl. Phys.* **A610**, 139C (1996).
- [100] R. Lacasse *et al.* (E877), *Quark matter '96. Proceedings, 12th International Conference on Ultrarelativistic Nucleus Nucleus Collisions, Heidelberg, Germany, May 20-24, 1996*, *Nucl. Phys.* **A610**, 153C (1996), arXiv:nucl-ex/9609001 [nucl-ex].
- [101] S. Ahmad *et al.*, *Phys. Lett.* **B382**, 35 (1996), [Erratum: *Phys. Lett.* **B386**, 496 (1996)].
- [102] J. Barrette *et al.* (E877), *Phys. Rev.* **C63**, 014902 (2001), arXiv:nucl-ex/0007007 [nucl-ex].
- [103] S. Albergo *et al.*, *Phys. Rev. Lett.* **88**, 062301 (2002).
- [104] C. Alt *et al.* (NA49), *Phys. Rev.* **C73**, 044910 (2006).
- [105] C. Alt *et al.* (NA49), *Phys. Rev.* **C77**, 024903 (2008), arXiv:0710.0118 [nucl-ex].
- [106] C. Alt *et al.* (NA49), *Phys. Rev.* **C78**, 034918 (2008), arXiv:0804.3770 [nucl-ex].
- [107] S. V. Afanasiev *et al.* (NA49), *Phys. Rev.* **C66**, 054902 (2002), arXiv:nucl-ex/0205002 [nucl-ex].
- [108] T. Anticic *et al.* (NA49), *Phys. Rev. Lett.* **93**, 022302 (2004), arXiv:nucl-ex/0311024 [nucl-ex].
- [109] T. Anticic *et al.* (NA49), *Phys. Rev.* **C83**, 014901 (2011), arXiv:1009.1747 [nucl-ex].

- [110] T. Anticic *et al.* (NA49), Phys. Rev. **C86**, 054903 (2012), arXiv:1207.0348 [nucl-ex].
- [111] L. Ahle *et al.* (E917, E866), Phys. Lett. **B476**, 1 (2000), arXiv:nucl-ex/9910008 [nucl-ex].
- [112] L. Ahle *et al.* (E917, E866), Phys. Lett. **B490**, 53 (2000), arXiv:nucl-ex/0008010 [nucl-ex].
- [113] I. G. Bearden *et al.* (BRAHMS), Phys. Rev. Lett. **94**, 162301 (2005), arXiv:nucl-ex/0403050 [nucl-ex].
- [114] I. Arsene *et al.* (BRAHMS), Phys. Rev. **C72**, 014908 (2005), arXiv:nucl-ex/0503010 [nucl-ex].
- [115] S. S. Adler *et al.* (PHENIX), Phys. Rev. **C69**, 034909 (2004), arXiv:nucl-ex/0307022 [nucl-ex].
- [116] G. Agakishiev *et al.* (STAR), Phys. Rev. Lett. **108**, 072301 (2012), arXiv:1107.2955 [nucl-ex].
- [117] R. Cutler and D. W. Sivers, Phys. Rev. **D17**, 196 (1978).
- [118] H. U. Bengtsson and G. Ingelman, Comput. Phys. Commun. **34**, 251 (1985).
- [119] M. Gell-Mann, Phys. Rev. **125**, 1067 (1962).
- [120] M. D. Schwartz, *Quantum Field Theory and the Standard Model* (Cambridge University Press, 2014).
- [121] R. Mertig, M. Böhm, and A. Denner, Computer Physics Communications **64**, 345 (1991).
- [122] V. Shtabovenko, R. Mertig, and F. Orellana, Computer Physics Communications **207**, 432 (2016).